## PAPER

Check for updates

# Electronic and optical properties of copper nanostructures for advanced applications†

Ragheb Khalil Bouriche, [ab] Douniazed Hannachi, *[cd] Amel Messai, [a] Christophe Morell, [e] Amor Azizi [b] and Henry Chermette *[e]

This study presents a comprehensive quantum computational investigation into the electronic structure, topological characteristics, and optical properties of two distinct series of copper hydride nanoclusters $[Cu_3L_3(H)_i(BH_4)_j]^+$ and $[Cu_3L_2(H)_i(BH_4)_j]^+$, where $i$ = 0 to 2 and $j$ = 0 and 1. The electronic stability and reactivity are systematically evaluated through chemical hardness and chemical potential analyses, revealing that $[Cu_3L_3(H)(BH_4)]^+$ exhibits the highest electronic stability, whereas $[Cu_3L_2(H)(BH_4)]^+$ presents the greatest susceptibility to electronic perturbations. To gain deeper insights into the nature of the M−L interactions, EDA-NOCV is employed, demonstrating pronounced covalent character in the bonding interaction between the copper center and the ligand fragments. The linear and nonlinear optical parameters have been rigorously computed under both static and dynamic regimes. Notably, $[Cu_3L_2(H)]^+$, $[Cu_3L_2(H)(BH_4)]^+$ and $[Cu_3L_3(H)]^+$ exhibit remarkably high first hyperpolarizability ($\beta_{tot}^0$), reaching up to 1500 a.u., whereas $Cu_3L_2(H)_2$ presents the lowest $\beta_{tot}^0$ value (166 a.u.). These significant variations in NLO activity are attributed to the intrinsic topological framework of the nanoclusters, coupled with kinetic and potential energy at the AIM critical points BCPs and RCPs, which critically modulate charge delocalization and electron density redistribution. Additionally, the pronounced polarizability anisotropy observed in $[Cu_3L_2(H)]^+$ and $[Cu_3L_2(H)(BH_4)]^+$ is identified as a key factor in increasing their NLO efficiency. Furthermore, second-order hyperpolarizability analysis indicates that $Cu_3L_3$ exhibits the highest value (173.48 × $10^4$ a.u.), whereas $Cu_3L_2(H)_2$ presents the lowest (5.688 × $10^4$ a.u.). Frequency-dependent analyses at laser wavelengths of 1340 nm and 1064 nm reveal a pronounced enhancement of dynamic hyperpolarizability over its static counterpart. Moreover, TD-DFT calculations validate the exceptional near-infrared (NIR) transparency of these nanoclusters. Specifically, nanoclusters $[Cu_3L_3(H)(BH_4)]^+$, $[Cu_3L_3(H)_2]^+$, $[Cu_3L_2(H)_2]^+$ and $[Cu_3L_2(H)]^+$ exhibit outstanding transparency across both the NIR and visible spectral regions, underscoring their potential for advanced applications in nonlinear optics and optoelectronic devices.

## Introduction

Since the discovery of the second harmonic generation (SHG) by Franken *et al.* in 1961,[1] numerous nonlinear optical (NLO)

[a] *Laboratory of Engineering and Advanced Materials Science (ISMA), Abbes Laghrour University, khenchela, 40000, Algeria*

[b] *Laboratory of Chemistry, Molecular Engineering and Nanostructures, Chemistry Department, Faculty of Science, Ferhat Abbas-Sétif University, Sétif 19000, Algeria*

[c] *Département de Chimie, Faculté des Sciences de la Matière, Université de Batna-1, Algeria*

[d] *Laboratoire d'Électrochimie, d'Ingénierie Moléculaire et de Catalyse Redox (LEIMCR), Département d'Enseignement de Base en Technologie, Faculté de Technologie, Université Ferhat Abbas, Sétif-1, Algeria. E-mail: douniazed_hannachi@univ-setif.dz, h_douniazed@yahoo.fr*

[e] *Institut des Sciences Analytiques, Université de Lyon, Université Claude Bernard Lyon 1, UMR CNRS 5280, 69622 Villeurbanne Cedex, France. E-mail: henry.chermette@univ-lyon1.fr*

† Electronic supplementary information (ESI) available. See DOI: https://doi.org/10.1039/d5nj01220a

phenomena have been identified, like third harmonic generation (THG), frequency mixing (sum and difference) and soliton propagation.[2,3] These phenomena have significant implications for advanced technological applications, such as photodynamic therapy,[4] biomedical imaging,[5,6] data storage, signal processing and quantum networks,[7] so forth. Moreover, NLO materials exhibit immense potential for diverse applications across multiple disciplines, including optoelectronic systems, photonic technologies, optical data processing, ultrafast optical communication networks, holographic visualization, and real-time image modulation, among others.[8–12] These developments continue to drive innovations in modern optical science and technology. As a result, the design and development of new high-performance NLO materials have garnered significant attention from researchers. Over the years, various compounds have been identified for their remarkable NLO responses, making them promising candidates for the design of excellent

NLO materials. Among them, one can cite the asymmetric coordination complexes,[13] molecules with donor–π-bridge–acceptor architectures, octupolar compounds,[14,15] X-type chiral π-conjugated oligomers, multi-decker sandwich clusters,[16,17] introducing diffuse excess electrons,[18] and so forth.

Copper hydrides have garnered significant interest due to their diverse applications in catalysis and materials science.[19] Their history dates back to 1844, when Wurtz first isolated a pyrophoric red solid, CuH.[20] Since then, a broad range of polynuclear copper(I) hydride complexes ($L_xCu_yH_n$) have been identified as crucial intermediates in various chemical transformations, including selective reductions, cycloaddition reactions,[21] and enantioselective functionalization processes such as hydroamination, hydroalkylation, and hydrobromination.[22–26] In addition to their catalytic significance, copper hydrides have also been investigated for their potential in hydrogen storage and $CO_2$ activation, among other applications.[27–30]

Theoretical and experimental investigations of hydride nanoclusters have consistently attracted considerable scientific interest.[31–33] In 2016, Li *et al.* conducted a comprehensive study on the synthesis, structural elucidation, and gas-phase reactivity of bis(diphenylphosphino)amino copper hydride nanoclusters.[34] These new complexes, represented as $Cu_3(X)(\mu_3\text{-H})$-$((PPh_2)_2NH)_3$, where $X = \mu_2\text{-Cl}$ and $\mu_3\text{-BH}_4$, were prepared and extensively characterized by high-resolution electrospray ionization mass spectrometry (ESI-MS), X-ray crystallography, nuclear magnetic resonance (NMR), and infrared (IR) spectroscopy. This study underscores the significant potential of copper hydride nanoclusters, which serve as a model system for the activation of $BH_4$, facilitating the formation of coordinated hydrides. These hydrides subsequently undergo $H_2$ elimination, promoting the generation of metallic clusters. Furthermore, the research provides crucial structural and mechanistic insights into polynuclear copper hydrides, laying the groundwork for an expanded understanding of their electronic properties and optical applications. Moreover, these findings open new avenues for the discovery of additional functionalities and potential applications of these nanoclusters in advanced materials science.

In this study, a comprehensive investigation is conducted utilizing quantum theory of atoms in molecules (QTAIM), energy decomposition analysis-natural orbitals for chemical valence (EDA-NOCV) and time-dependent density functional theory (TD-DFT) to study two distinct series of copper hydride nanoclusters designed and synthesized by Li *et al.*,[34] namely $[Cu_3L_3(H)_i(BH_4)_j]^+$ and $[Cu_3L_2(H)_i(BH_4)_j]^+$, where $i = 0$ to 2 and $j = 0$ or 1 (ranging from **A** to **H**), as illustrated in Fig. 1. In this study, two specific cases were excluded from consideration. The first case, corresponding to $i = 2$ and $j = 1$, was eliminated due to severe steric congestion and pronounced geometric distortion, which rendered the incorporation of a second hydride ligand both energetically unfavourable and structurally impractical. The second case, $i = 1$ and $j = 1$, was excluded because the optimized geometry of the $[Cu_3L_2(BH_4)]^+$ nanocomplex exhibited complete structural distortion, thereby preventing its use in meaningful comparative analysis.
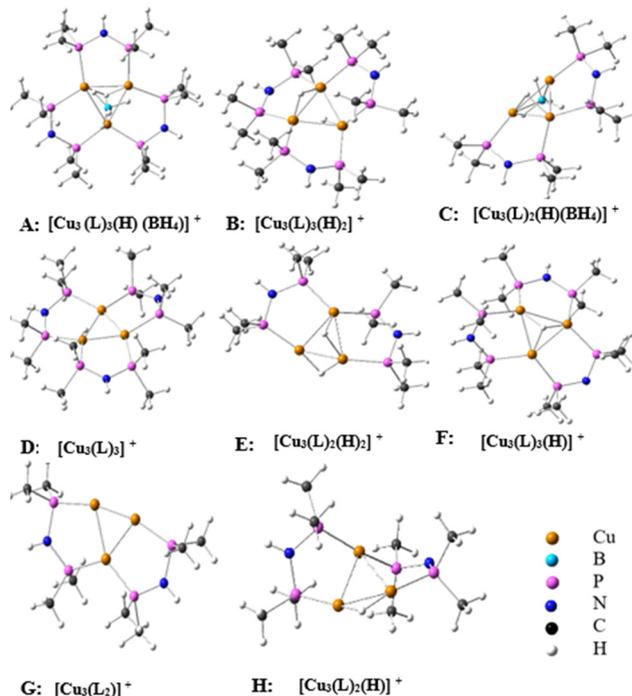


Fig. 1 Chemical structures of the studied copper hydride nanoclusters.

The primary objective of this study is to predict the optical properties of these nanoclusters and to systematically assess the impact of hydride units (H), $BH_4$ ligands, and the bis-(dimethylphosphino)amine (dmpa) ligand (L) on their nonlinear optical (NLO) responses and electronic structures. Notably, to achieve this DFT calculation, the bis(diphenylphosphino)amine (dppa) ligand, as identified in experimental results,[34] was systematically substituted with bis(dimethylphosphino)amine (dmpa = L). This strategic modification enables a thorough investigation of the influence of L, H, and $BH_4$ on the electronic structure and optical properties of the nanoclusters, providing deeper insight into their fundamental characteristics. To enable a precise comparison between the two nanocluster series, $[Cu_3L_3]^+$ and $[Cu_3L_2]^+$ (**D** and **G**, respectively) were designated as reference compounds.

## Computational details

The starting point for this quantum chemical calculation was the optimized geometries of $[Cu_3L_k(H)_i(BH_4)_j]^+$, where $k = 1, 2$; $i = 0$ to 2; $j = 0$ and 1 (Fig. 1), performed by Li and co-workers.[34] To evaluate the linear and nonlinear optical properties of these hydride copper nanoclusters (Fig. 1) we used the M06-2X functional,[35] a global hybrid functional with 54% Hartree–Fock exchange. This method has been previously utilized in similar studies on transition metal complexes, highlighting its accuracy and reliability in quantum chemical calculations.[36–40] A split-valence basis set, 6-31+G(d), incorporating diffuse and polarization functions, was applied to all atoms. However, for the copper atoms, the Stuttgart–Dresden effective core potentials (ECPs) with SDD basis sets were used.[41,42] Scalar relativistic effects

were addressed through the use of ECPs. This calculation was performed with Gaussian16.[43]

On the other hand, Amsterdam density functional (ADF2023)[44] software was used for the QTAIM study[45–48] and EDA-NOCV analyses.[49,50] This calculation used the PBE[51] functional with the triple-ζ plus polarization (TZP) basis set, with numerical quality "VeryGood". The integration grid was the Becke Grid with quality "VeryGood".[52] Relativistic corrections were taken into account with the use of the relativistic scalar zero-order-regular approximation (ZORA);[53,54] no dispersion correction was used.

The average polarizability ($\alpha$) and its anisotropy ($\Delta\alpha$) are defined through the relations[55]

$$\alpha = \frac{1}{3}(\alpha_{xx} + \alpha_{yy} + \alpha_{zz}) \tag{1}$$

$$\Delta\alpha = \left[\frac{1}{2}\left\{(\alpha_{xx} - \alpha_{yy})^2 + (\alpha_{yy} - \alpha_{zz})^2 + (\alpha_{zz} - \alpha_{xx})^2 + 6(\alpha_{xy}^2 + \alpha_{xz}^2 + \alpha_{yz}^2)\right\}\right]^{1/2} \tag{2}$$

The static first hyperpolarizability is outlined as follows:

$$\beta_{\text{tot}}^0 = \sqrt[2]{\beta_x^2 + \beta_y^2 + \beta_z^2} \tag{3}$$

where $\beta_x = \beta_{xxx} + \beta_{xyy} + \beta_{xzz}$, $\beta_y = \beta_{yyy} + \beta_{xxy} + \beta_{yzz}$ and $\beta_z = \beta_{zzz} + \beta_{zyy} + \beta_{xxz}$.

The total magnitude of static second hyperpolarizability $\gamma$ is estimated as[56–58]

$$\gamma_{\text{tot}}^0 = \sqrt{\gamma_x^2 + \gamma_y^2 + \gamma_z^2} \tag{4}$$

where $\gamma_i = \frac{1}{15}\sum_j (\gamma_{ijji} + \gamma_{ijij} + \gamma_{iijj})$ $i,j = \{x, y, z\}$

On the other hand, the quadratic nonlinear refractive index ($n_2$) is calculated from the second hyperpolarizability coefficients, utilizing the following equation:[59]

$$n_2 \text{ (cm}^2 \text{ W}^{-1}) = 8.28 \times 10^{-23} \gamma^{\text{DFWM}} \text{ (a.u.)} \tag{5}$$

The degenerate four-wave mixing (DFWM) values are calculated using eqn (6) provided below:[60]

$$\gamma^{\text{DFWM}}(-\omega; \omega, -\omega, \omega) \approx \left(\frac{1}{3}\right)\gamma(-2\omega; \omega, \omega, 0) + \gamma(-\omega; \omega, 0, 0) \\ - \left(\frac{1}{3}\right)\gamma(0; 0, 0, 0) \tag{6}$$

In this study, the hyper-Rayleigh scattering (HRS), denoted as $\beta_{\text{HRS}}$, is examined. As well this parameter is directly related with the intensity of HRS when nonpolarized light is used and the scattered light is detected in a plane-polarized state perpendicular to the propagation plane. $\beta_{\text{HRS}}$ is given by[61–63]

$$\langle \beta_{\text{HRS}} \rangle = \sqrt{\{\langle \beta_{ZZZ}^2 \rangle + \langle \beta_{XZZ}^2 \rangle\}} \tag{7}$$

where $\langle \beta_{ZZZ}^2 \rangle$ and $\langle \beta_{XZZ}^2 \rangle$ denote the orientational averages of $\beta$ tensor components, which can be calculated as follows:

$$\langle \beta_{ZZZ}^2 \rangle = \frac{1}{7}\sum_i^{x,y,z} \beta_{iii}^2 + \frac{4}{35}\sum_{i \neq J}^{x,y,z} \beta_{iiJ}^2 + \frac{2}{35}\sum_{i \neq J}^{x,y,z} \beta_{iii}\beta_{ijj} \\ + \frac{4}{35}\sum_{i \neq J}^{x,y,z} \beta_{jii}\beta_{iij} + \frac{4}{35}\sum_{i \neq J}^{x,y,z} \beta_{iii}\beta_{jji} + \frac{1}{35}\sum_{i \neq J}^{x,y,z} \beta_{Jii}^2 \\ + \frac{4}{105}\sum_{i \neq J \neq k}^{x,y,z} \beta_{iij}\beta_{jkk} + \frac{1}{105}\sum_{i \neq J \neq k}^{x,y,z} \beta_{jii}\beta_{jkk} \\ + \frac{4}{105}\sum_{i \neq J \neq k}^{x,y,z} \beta_{iij}\beta_{kkj} + \frac{2}{105}\sum_{i \neq J \neq k}^{x,y,z} \beta_{ijk}^2 + \frac{4}{105}\sum_{i \neq J \neq k}^{x,y,z} \beta_{ijk}\beta_{jik}$$

$$\langle \beta_{XZZ}^2 \rangle = \frac{1}{35}\sum_i^{x,y,z} \beta_{iii}^2 + \frac{4}{105}\sum_{i \neq J}^{x,y,z} \beta_{iii}\beta_{ijj} - \frac{2}{35}\sum_{i \neq J}^{x,y,z} \beta_{iii}\beta_{jji} \\ + \frac{8}{105}\sum_{i \neq J}^{x,y,z} \beta_{iiJ}^2 + \frac{3}{35}\sum_{i \neq J}^{x,y,z} \beta_{ijj}^2 - \frac{2}{35}\sum_{i \neq J}^{x,y,z} \beta_{iij}\beta_{jii} \\ + \frac{1}{35}\sum_{i \neq J \neq k}^{x,y,z} \beta_{ijj}\beta_{ikk} - \frac{2}{105}\sum_{i \neq J \neq k}^{x,y,z} \beta_{iik}\beta_{jjk} \\ + \frac{2}{35}\sum_{i \neq J \neq k}^{x,y,z} \beta_{ijk}^2 - \frac{2}{105}\sum_{i \neq J \neq k}^{x,y,z} \beta_{iij}\beta_{jkk} - \frac{2}{105}\sum_{i \neq J \neq k}^{x,y,z} \beta_{ijk}\beta_{jik}$$

Additionally, depolarization ratios (DR) provide valuable insights into the chromophore geometry, which significantly influences the compound's NLO properties. In an ideal one-dimensional system, the DR is typically equal to 5, while an octupolar molecule exhibits a DR of 1.5.

$$\text{DR} = \frac{\langle \beta_{ZZZ}^2 \rangle}{\langle \beta_{XZZ}^2 \rangle} \tag{8}$$

In NLO materials, the degree of charge transfer (CT) plays a crucial role in determining the NLO response. Electron excitation can be described as the movement of an electron and the formation of a hole in the region it vacates. To quantify CT length, the $D$ index is defined as the distance between the centroids of the electron and hole, as given by the following equation:

$$D \text{ index} = [(D_x)^2 + (D_y)^2 + (D_z)^2]^{1/2} \tag{9}$$

where $D_x = |X_{\text{ele}} - X_{\text{hole}}|$, $D_Y = |Y_{\text{ele}} - Y_{\text{hole}}|$ and $D_Z = |Z_{\text{ele}} - Z_{\text{hole}}|$.

Additionally, $t_{\text{index}}$ is introduced to evaluate the separation degree between the electron and hole in the CT direction. A $t_{\text{index}}$ value below zero indicates minimal separation between the electron and hole, whereas a distinctly positive value signifies a noticeable separation between them.

$$t_{\text{index}} = D_{\text{CT}} - H_{\text{CT}} \tag{10}$$

and

$$H_{\text{CT}} = |H \cdot u_{\text{CT}}| \tag{11}$$

where $H_{CT}$ is the degree of spatial extension of hole and electron distribution in the CT direction, and $u_{CT}$ denotes the unit vector in CT.

On the other hand, the variations of dipole moment of the excited state with respect to the ground state in $X$, $Y$ and $Z$ directions can be calculated as

$$\Delta\mu = \sqrt{\Delta\mu_x^2 + \Delta\mu_x^2 + \Delta\mu_x^2} \qquad (12)$$

where $\Delta\mu_x = (X_{ele} - X_{hole})$, $\Delta\mu_y = -(Y_{ele} - Y_{hole})$ and $\Delta\mu_z = -(Z_{ele} - Z_{hole})$.

In our study, the crucial excited-state wavefunctions have been determined by natural transition orbitals (NTOs), which represent the electronic transition density matrix in terms of an "excited particle" and an "empty hole." Additionally, charge transfer (CT) indices were computed using the MULTIWFN program.[64]

On the other hand, the effect of solvent environments on the nonlinear optical responses of the **A** nanocluster was investigated using the conductor-like polarizable continuum model (CPCM).[65,66] Geometry optimizations of the **A** nanocluster were performed in solvent phases (water, methanol, and benzene) employing CPCM at the same level of theory as used for the gas-phase calculations.[34]

According to the literature, experimental and calculated values of nonlinear optical parameters exhibit a consistent trend. In other words, an increase in the experimental hyperpolarizability of some compound is reliably accompanied by a corresponding rise in theoretical predictions. This emphasizes that the computational method does not influence the relative ordering of properties within a series of molecules but significantly impacts the absolute magnitude of the computed values.[36–40,67–69]

# Results and discussion

### Structural parameters

The geometric parameters of copper hydride nanocluster **A** were optimized in the gas phase and in three distinct solvent environments (water, methanol, and benzene) using the CPCM to simulate solvation effects. The calculated angle and bond lengths, summarized in Table 1, were rigorously compared with experimental crystallographic data of **A**.[34] Overall, the X–Cu and

**Table 1** The average bond lengths X–Cu, Cu–B and Cu–hydride (Å), distance value X–hydride and B–X (Å), and angle B–X–hydride (°) in gas and solvent

|  | Exp. | Gas | Water | Methanol | Benzene |
|---|---|---|---|---|---|
| X–hydride | 0.866 | 0.925 | 0.855 | 0.862 | 0.870 |
| X–B | 2.072 | 2.218 | 2.219 | 2.215 | 2.196 |
| X–Cu | 1.533 | 1.509 | 1.528 | 1.525 | 1.521 |
| Cu–B | 2.577 | 2.681 | 2.694 | 2.689 | 2.671 |
| Cu–hydride | 1.760 | 1.707 | 1.751 | 1.751 | 1.752 |
| B–X–hydride | 178 | 180 | 180 | 179 | 180 |

Exp: experimental data from ref. 34. X: centroid of the triangular arrangement of copper atoms.

Cu–hydride distances are slightly underestimated across all phases. We note that the X–Cu bond is shorter by approximately 0.006 Å in both water and methanol, 0.012 Å in benzene and 0.024 Å in the gas phase. The Cu–hydride bond length deviates from the experimental value by 0.053 Å in the gas phase, while in solvent environments this difference is reduced to 0.008 Å. Conversely, the X–B and Cu–B bond lengths are consistently overestimated, with elongations of ∼0.125 Å in the gas phase, and 0.109 and 0.129 Å in polar and apolar solvents, respectively. Moreover, the computed distance between the hydride and the centroid of the copper triangle (X) is notably overestimated in the gas phase (+0.059 Å) and to a lesser extent in benzene (+0.004 Å). In contrast, a slight contraction is observed in polar media, with reductions of 0.011 Å in water and 0.004 Å in methanol. The calculated bond angles in both gas phase and solvent environments show good agreement with experimental data. In general, the slight deviations observed in the geometric parameters across different media remain within acceptable limits and do not significantly alter the overall molecular geometry of nanocluster **A**.

### Electronic properties

Frontier molecular orbital (FMO) analysis is utilized to investigate the optical, chemical reactivity and electronic properties of the nanoclusters $[Cu_3L_k(H)_i(BH_4)_j]^+$ ($k = 2, 3$; $i = 0, 1$ or $2$; $j = 0$ or $1$). The energies of the FMOs (HOMO and LUMO) are fundamental in calculating chemical potential ($\mu$) and chemical hardness ($\eta$), which provide crucial insights into the stability and reactivity of the systems. The chemical potential is defined as $\mu = (E_{HOMO} + E_{LUMO})/2$ and the chemical hardness is given by $\eta = E_{LUMO} - E_{HOMO}$.[70–73] Compounds exhibiting higher chemical potential values tend to act as electron donors, indicating an enhanced ability to donate electrons. Conversely, those with lower chemical hardness values are associated with reduced stability and increased reactivity, signifying that these systems are more susceptible to charge transfer and more likely to undergo chemical reactions.

Fig. 2 presents the chemical hardness and chemical potential of nanoclusters **A** to **H**, as well as their HOMO–LUMO orbitals. A comparison of chemical hardness ($\eta$) among
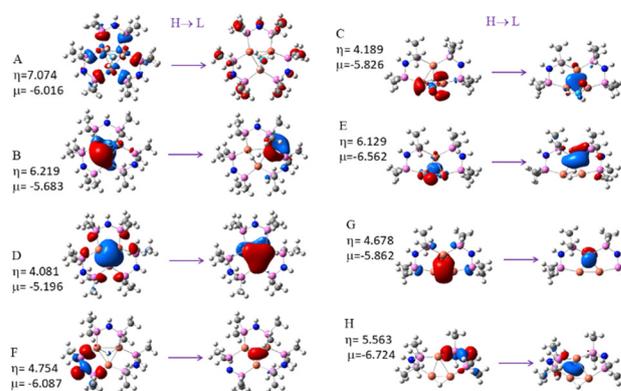


**Fig. 2** Shapes of the HOMO and LUMO, chemical potential ($\mu$, eV) and chemical hardness ($\eta$, eV) of nanoclusters **A** to **H**.

nanoclusters **A** to **H** reveals significant variations in their electronic stability. For the $[Cu_3L_3(H)_i(BH_4)_j]^+$ series ($k = 3$), nanocluster **A** exhibits the highest $\eta$ (7.074 eV), indicating the greatest stability and resistance to charge transfer, followed by **B** (6.219 eV), **F** (4.754 eV), and **D** (4.081 eV). This trend suggests that the presence of $BH_4$ and hydride fragments enhances the stability of the nanoclusters compared to those with only two hydrides or one hydride. Conversely, for the $Cu_3L_2(H)_i(BH_4)_j$ series ($k = 2$), the trend reverses, with nanocluster **E** showing the highest $\eta$ among **H**, **G**, and **C**, indicating that the two hydride fragments in **E** contribute more significantly to stability than the combination of one hydride or hydride with $BH_4$ in **C**. This difference in trends between the two series can be attributed to the varying number of L ligands, which play a crucial role in modulating the electronic stability of the nanoclusters. In summary, the hardness trend from highest to lowest is **A** > **B** > **E** > **H** > **F** > **G** > **C** > **D**, with **A** being the most stable and **D** the most reactive, highlighting the inverse relationship between hardness and reactivity across the nanoclusters.

Regarding the chemical potential ($\mu$), nanoclusters **H**, **E**, **F**, and **A** exhibit the most negative $\mu$ values ($-6.724$, $-6.562$, $-6.087$, and $-6.016$ eV, respectively), indicating a lower tendency to release electrons, and thus enhanced stability. These are followed by **G** ($-5.862$ eV), **C** ($-5.826$ eV) and **B** ($-5.683$ eV). In contrast, nanocluster **D** has the least negative $\mu$ ($-5.196$ eV), suggesting that it is the most nucleophilic and has a greater tendency to donate electrons. The overall order of chemical potential from most negative to least negative for both series is **F** $\approx$ **A** > **B** > **D** and **H** > **E** > **G** $\approx$ **C**, suggesting that nanoclusters without hydride fragments possess a greater electron-donating ability.

## Topological study

To investigate the nature of bonding interactions between copper atoms (Cu), $BH_4$ and L ligands and hydride atoms (Fig. 1), a comprehensive topological analysis of the electron density was performed on the studied nanoclusters (**A** to **H**). This analysis was conducted using the framework of the quantum theory of atoms in molecules (QTAIM), as formulated by Bader.[46,47,74–76] Calculations were carried out using the ADF23 software package,[77] developed by Baerends et al.[30]

Within the QTAIM framework, critical points—such as bond critical points (BCPs) and ring critical points (RCPs)—are identified as positions where the gradient of the electron density vanishes. These critical points are characterized by several parameters, including the electron density ($\rho$), its Laplacian ($\nabla^2(\rho)$), total energy density ($H$), kinetic energy density ($G$), and potential energy density ($V$). These descriptors provide insights into the nature of bonding and electronic interactions within the system. The computed parameters for nanoclusters **A** through **H** are systematically presented in tables and depicted in figures, providing a comprehensive visualization of the electron density topology. In these graphical representations, green circles indicate ring critical points (RCPs), while red circles correspond to bond critical points (BCPs).

The QTAIM analysis of nanocluster **A** provides detailed insights into its electronic structure and bonding interactions.

**Table 2** Topological parameters calculated for investigated nanocluster **A** BCPs and RCPs

| | $\rho$ | $\nabla^2(\rho)$ | $G$ | $V$ | $H$ |
|---|---|---|---|---|---|
| RCP1 | 0.0144 | 0.0333 | 0.0080 | −0.0076 | 0.0003 |
| RCP2 | 0.0143 | 0.0333 | 0.0080 | −0.0076 | 0.0003 |
| RCP3 | 0.0143 | 0.0332 | 0.0080 | −0.0076 | 0.0003 |
| RCP1′ | 0.0209 | 0.0410 | 0.0114 | −0.0126 | 0.0011 |
| RCP2′ | 0.0210 | 0.0411 | 0.0114 | −0.0126 | −0.0012 |
| RCP3′ | 0.0210 | 0.0410 | 0.0114 | −0.0126 | −0.0012 |
| RCP″ | 0.0201 | 0.0370 | 0.0104 | −0.0116 | −0.0012 |
| BCP1 | 0.0681 | 0.1521 | 0.0579 | −0.0779 | −0.0199 |
| BCP2 | 0.0678 | 0.1517 | 0.0576 | −0.0773 | −0.0197 |
| BCP3 | 0.0679 | 0.1517 | 0.0577 | −0.0775 | −0.0198 |
| BCP1′ | 0.1419 | −0.1877 | 0.0796 | −0.2061 | −0.1265 |
| BCP2′ | 0.1420 | −0.1885 | 0.0796 | −0.2063 | −0.1267 |
| BCP3′ | 0.1418 | −0.1874 | 0.0795 | −0.206 | −0.1264 |

RCP: Cu–Cu–P–N–P; RCP′: Cu–Cu–H–B–H; RCP″: 3Cu-H-$BH_4$. BCP: Cu$\cdots$H; BCP′: Cu$\cdots$H–B. Values are given in atomic units (a.u.).
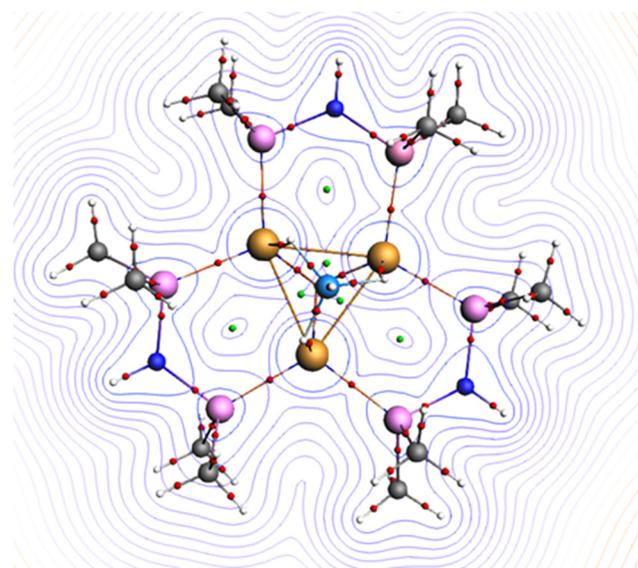


**Fig. 3** Molecular topology of nanocluster **A**.

From the results in Table 2 and Fig. 3 we can note that the RCPs associated with Cu–Cu–P–N–P (RCP1–RCP3), the low electron density ($\rho \approx 0.0143$–$0.0144$ a.u.) and positive Laplacian ($\nabla^2\rho \approx 0.0332$–$0.0333$ a.u.) indicate weak, closed-shell interactions. Conversely, RCPs linked to Cu–Cu–H–B–H (RCP1′–RCP3′) exhibit higher $\rho$ ($\approx 0.0209$–$0.0210$ a.u.) and ($\nabla^2(\rho)$) ($0.0410$–$0.0411$ a.u.), suggesting stronger interactions with slight covalent contributions, as evidenced by negative total energy densities ($H \approx -0.0012$ a.u.).

The nature of hydrogen bonding interactions is classified according to the criteria established by Rozas et al.[78] Based on the parameters at the BCPs, two distinct types of hydrogen bonds are identified. The Cu$\cdots$H interactions (BCP1–BCP3) exhibit moderate electron density ($\rho \approx 0.0678$–$0.0681$ a.u.) and positive Laplacian values ($\nabla^2(\rho) \approx 0.152$ a.u.), accompanied by negative total energy densities ($H \approx -0.0197$ to $-0.0198$ a.u.). These characteristics align with moderate hydrogen bonds, which display mixed electrostatic and covalent

character. In contrast, the Cu···H–B interactions (BCP1′–BCP3′) are characterized by significantly higher electron density ($\rho \approx 0.142$ a.u.) and negative Laplacian values ($\nabla^2(\rho) \approx -0.187$ a.u.), along with highly negative total energy densities ($H \approx -0.126$ a.u.). These parameters are indicative of strong hydrogen bonds with a covalent-like character.

Overall, the hydrogen bonding framework in nanocluster **A** showcases a dual nature, with moderate Cu···H bonds contributing to structural flexibility and strong Cu···H–B bonds providing stability through robust covalent interactions.

For nanocluster **B**, it can be observed that RCP1, RCP2 and RCP3 exhibit low electron density ($\rho \approx 0.014$–$0.015$ a.u.) and positive Laplacian ($\nabla^2\rho \approx 0.034$–$0.038$ a.u.), indicating weak, closed-shell interactions (Table 3 and Fig. 4). The RCP′ reveals $\rho \approx 0.043$ a.u. and $\nabla^2(\rho) \approx 0.086$ a.u., indicating closed-shell interactions. The Cu···H interactions (BCP1–BCP3) display electron density values ranging from $\rho = 0.0532$ to $0.0773$ a.u., with positive Laplacian values ($\nabla^2(\rho) = 0.1200$ to $0.1480$ a.u.) and negative total energy densities ($H = -0.028$ to $-0.012$ a.u.). These parameters indicate the presence of moderate hydrogen bonding with a hybrid electrostatic–covalent

**Table 3** Topological parameters calculated for investigated nanocluster **B** BCPs and RCPs

| | $\rho$ | $\nabla^2(\rho)$ | $G$ | $V$ | $H$ |
|---|---|---|---|---|---|
| RCP1 | 0.0147 | 0.0348 | 0.0083 | −0.0080 | 0.0003 |
| RCP2 | 0.0153 | 0.0342 | 0.0084 | −0.0082 | 0.0001 |
| RCP3 | 0.0148 | 0.0385 | 0.0090 | −0.0083 | 0.0006 |
| RCP1′ | 0.0427 | 0.0860 | 0.0293 | −0.0371 | −0.0078 |
| BCP1 | 0.0532 | 0.1200 | 0.0416 | −0.0533 | −0.0116 |
| BCP2 | 0.0773 | 0.1480 | 0.0650 | −0.0929 | −0.0280 |
| BCP3 | 0.0565 | 0.1246 | 0.0447 | −0.0582 | −0.0135 |
| BCP1′ | 0.0706 | 0.1373 | 0.0575 | −0.0807 | −0.0232 |
| BCP2′ | 0.0686 | 0.1367 | 0.0558 | −0.0774 | −0.0216 |

RCP: Cu–Cu–P–N–P; RCP′: Cu–H–Cu–H. BCP: Cu···H (H between 3 Cu); BCP′: Cu···H (H between 2 Cu). Values are given in atomic units (a.u.).
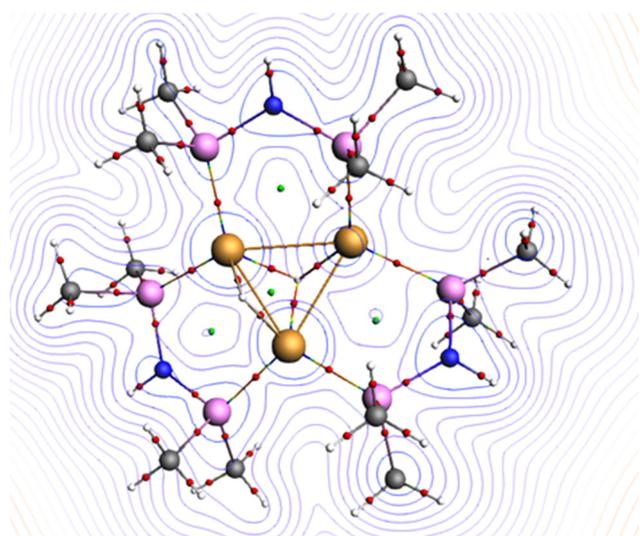
**Table 4** Topological parameters calculated for investigated nanocluster **C** BCPs and RCPs

| | $\rho$ | $\nabla^2(\rho)$ | $G$ | $V$ | $H$ |
|---|---|---|---|---|---|
| RCP1 | 0.0173 | 0.0444 | 0.0107 | −0.0103 | 0.0004 |
| RCP2 | 0.0318 | 0.0612 | 0.0194 | −0.0235 | −0.0041 |
| RCP3 | 0.0152 | 0.0386 | 0.0091 | −0.0086 | 0.0005 |
| BCP1 | 0.0626 | 0.1426 | 0.0521 | −0.0686 | −0.0165 |
| BCP2 | 0.0691 | 0.1483 | 0.0581 | −0.0791 | −0.0210 |
| BCP3 | 0.0700 | 0.1526 | 0.0596 | −0.0811 | −0.0215 |
| BCP1′ | 0.0652 | 0.1860 | 0.0613 | −0.0762 | −0.0149 |
| BCP2′ | 0.0660 | 0.1841 | 0.0616 | −0.0770 | −0.0155 |

RCP: Cu–Cu–P–N–P; RCP′: Cu–BH₄–Cu. BCP: 3Cu···H; BCP′: Cu···H–B. Values are given in atomic units (a.u.).

character. A similar character is observed in BCP′1 and BCP′2 (where $\rho = 0.0706$ and $0.0686$ a.u., $\nabla^2(\rho) = 0.1373$ and $0.1367$ a.u. and $H = -0.0232$ and $-0.0216$ a.u., respectively).

From Table 4, the RCPs associated with Cu–Cu–P–N–P (RCP1–RCP3) exhibit low $\rho$ ($0.0152$–$0.0318$ a.u.) and positive $\nabla^2(\rho)$ ($0.0386$–$0.0612$ a.u.), indicating weak closed-shell interactions. The Cu···H interactions (BCP1–BCP3) show $\rho = 0.062$ to $0.070$ a.u., $\nabla^2\rho = 0.142$ to $0.152$ a.u., and $H = -0.02146$ to $-0.0165$ a.u., suggesting moderate hydrogen bonding with a mixed electrostatic–covalent character. A similar trend is observed for BCP′1 and BCP′2, characterized by $\rho = 0.065$ and $0.066$ a.u., $\nabla^2\rho = 0.186$ and $0.184$ a.u., and $H = -0.014$ and $-0.015$ a.u., respectively (Fig. 5).

For nanocluster **D**, Table 5 highlights distinct bonding characteristics in RCPs, where Cu–Cu–P–N–P (RCP1–RCP3) interactions exhibit $\rho = 0.0152$–$0.0153$ a.u. and $\Delta^2\rho = 0.0371$–$0.0372$ a.u., indicating weak closed-shell interactions. In contrast, RCP1′ presents a higher electron density ($\rho = 0.0403$ a.u.) and a lower Laplacian ($\Delta^2\rho = 0.0304$ a.u.), suggesting a stronger yet electrostatically influenced bond (see Fig. 6).

For **E**, the data in Table 6 indicate that RCPs (Cu–Cu–P–N–P) exhibit low $\rho$ ($0.0131$–$0.0167$ a.u.) and positive $\Delta^2\rho$, suggesting weak closed-shell interactions. In contrast, BCPs (Cu···H) show higher $\rho$ ($0.0663$–$0.0801$ a.u.) and negative $H$, indicating moderate hydrogen bonding with a mixed electrostatic–covalent
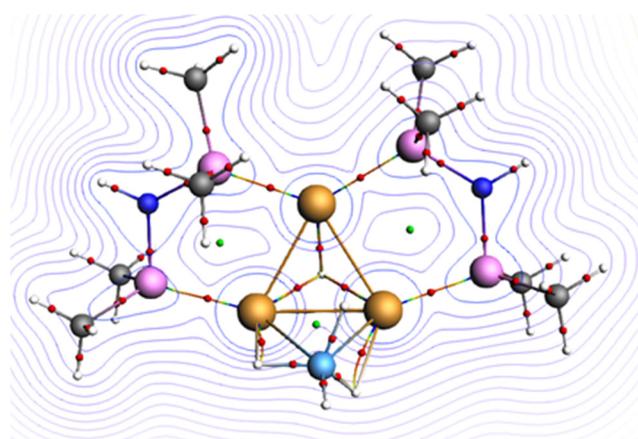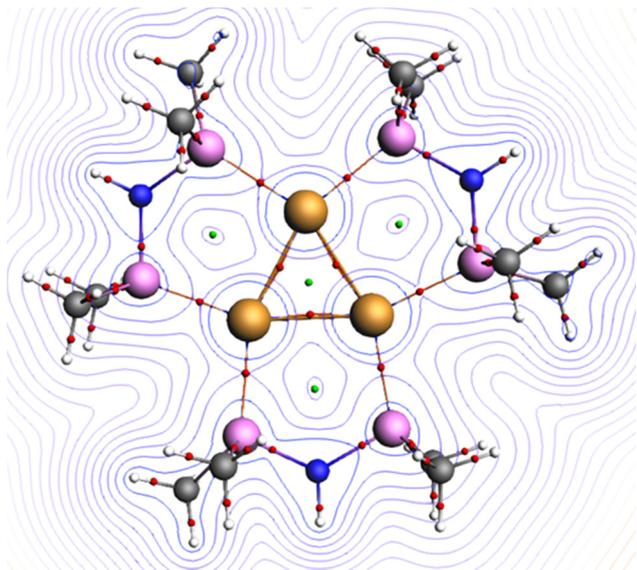


Fig. 4 Molecular topology of nanocluster **B**.



Fig. 5 Molecular topology of nanocluster **C**.

**Table 5** Topological parameters calculated for investigated nanocluster **D** BCPs and RCPs

| | $\rho$ | $\nabla^2(\rho)$ | $G$ | $V$ | $H$ |
|---|---|---|---|---|---|
| RCP1 | 0.0152 | 0.0371 | 0.0088 | −0.0085 | 0.0004 |
| RCP2 | 0.0153 | 0.0372 | 0.0089 | −0.0085 | 0.0004 |
| RCP3 | 0.0153 | 0.0371 | 0.0089 | −0.0085 | 0.0004 |
| RCP1′ | 0.0403 | 0.0304 | 0.0187 | −0.0298 | −0.0111 |

RCP: Cu–Cu–P–N–P; RCP′: trinuclear copper. Values are given in atomic units (a.u.).



Fig. 6 Molecular topology of nanocluster **D**.

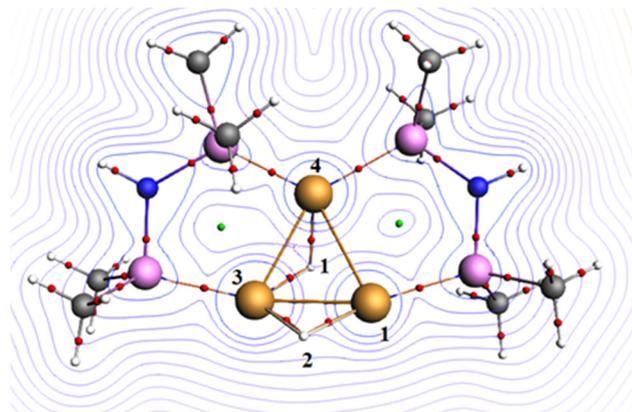**Table 6** Topological parameters calculated for investigated nanocluster **E** BCPs and RCPs

| | $\rho$ | $\nabla^2(\rho)$ | $G$ | $V$ | $H$ |
|---|---|---|---|---|---|
| RCP1 | 0.0131 | 0.0325 | 0.0075 | −0.0069 | 0.0006 |
| RCP2 | 0.0167 | 0.0432 | 0.0103 | −0.0098 | 0.0005 |
| BCP1 | 0.0801 | 0.1550 | 0.0686 | −0.0984 | −0.0298 |
| BCP2 | 0.0663 | 0.1361 | 0.0539 | −0.0737 | −0.0199 |
| BCP′1 | 0.0764 | 0.1558 | 0.0655 | −0.0920 | −0.0265 |
| BCP′2 | 0.0880 | 0.1530 | 0.0754 | −0.1126 | −0.0372 |

RCP: Cu–Cu–P–N–P. BCP1: Cu3···H1; BCP2: Cu4···H1; BCP′1: Cu3···H2; BCP′2: Cu1···H2. Values are given in atomic units (a.u.).



Fig. 7 Molecular topology of nanocluster **E**.

**Table 7** Topological parameters calculated for investigated nanocluster **F** BCPs and RCPs

| | $\rho$ | $\nabla^2(\rho)$ | $G$ | $V$ | $H$ |
|---|---|---|---|---|---|
| RCP1 | 0.0155 | 0.0357 | 0.0087 | −0.0085 | 0.0002 |
| RCP2 | 0.0144 | 0.0302 | 0.0075 | −0.0074 | 0.00007 |
| RCP3 | 0.0169 | 0.0402 | 0.0100 | −0.0097 | 0.0001 |
| BCP1 | 0.0766 | 0.1582 | 0.0660 | −0.9257 | −0.2650 |
| BCP2 | 0.0663 | 0.1527 | 0.0567 | −0.0751 | −0.0185 |
| BCP3 | 0.0668 | 0.1504 | 0.0567 | −0.0758 | −0.0191 |

RCP: Cu–Cu–P–N–P; BCP: 3Cu···H. Values are given in atomic units (a.u.).



Fig. 8 Molecular topology of nanocluster **F**.

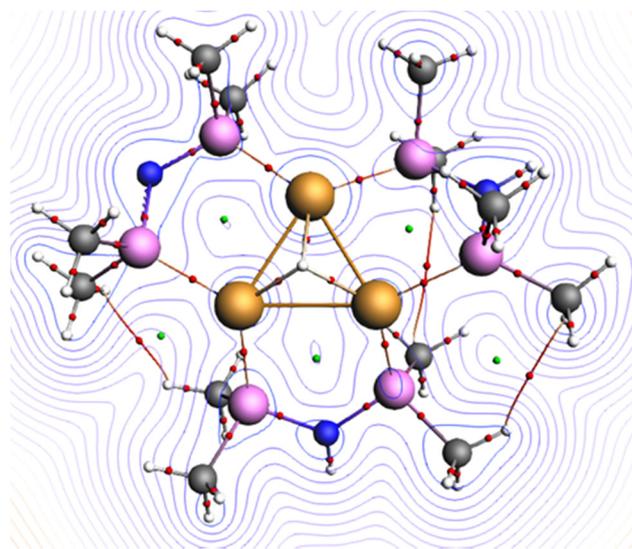nature, where BCP′2 (Cu1···H2) is the strongest interaction (see Fig. 7).

For nanocluster **F**, the data in Table 7 show that RCPs (Cu–Cu–P–N–P) have low $\rho$ (0.0144–0.0169 a.u.) and positive $\nabla^2\rho$, indicating weak closed-shell interactions. In contrast, BCPs (3Cu···H) exhibit higher $\rho$ (0.0663–0.0766 a.u.) and negative $H$, suggesting moderate hydrogen bonding with a mixed electrostatic–covalent nature, where BCP1 (3Cu···H) represents the strongest interaction in this nanocluster (see Fig. 8).

In the case of nanocluster **G**, the data in Table 8 indicate that RCP1 and RCP′ exhibit low $\rho$ ($\rho < 0.1$ a.u.) and positive $\Delta^2\rho$, suggesting weak closed-shell interactions. In contrast, RCP2

presents a negative $H$ (−0.0108 a.u.) and positive $\Delta^2\rho$ (0.041 a.u.), indicating a stronger interaction with partial covalent character.

A comparison between nanoclusters **G** and **D** reveals that **G** exhibits stronger Cu–Cu–P–N–P interactions than **D**, as evidenced by RCP2 ($\rho = 0.0415$ a.u., $H = -0.0108$ a.u.), which indicates greater covalent character than the corresponding interaction in **D** ($\rho = 0.015$ a.u.). However, RCP1′ remains

**Table 8** Topological parameters calculated for investigated nanocluster **G** BCPs and RCPs
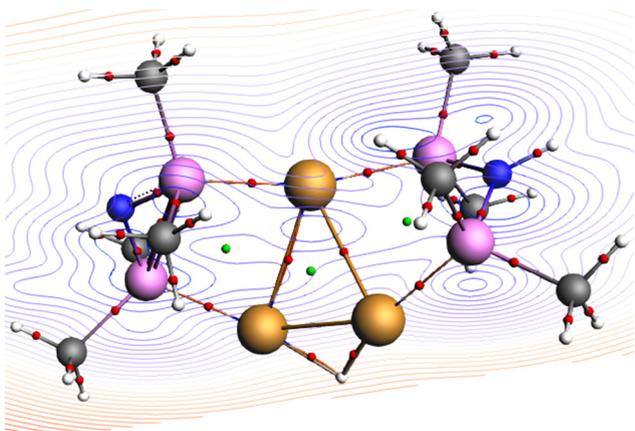
|       | $\rho$ | $\nabla^2(\rho)$ | $G$ | $V$ | $H$ |
|-------|--------|------------------|-----|-----|-----|
| RCP1  | 0.0151 | 0.0420 | 0.0096 | −0.0088 | 0.0008 |
| RCP2  | 0.0415 | 0.0419 | 0.0213 | −0.0321 | −0.0108 |
| RCP1′ | 0.0150 | 0.0418 | 0.0096 | −0.0087 | 0.0008 |

RCP: Cu–Cu–P–N–P; RCP′: trinuclear copper. Values are given in atomic units (a.u.).
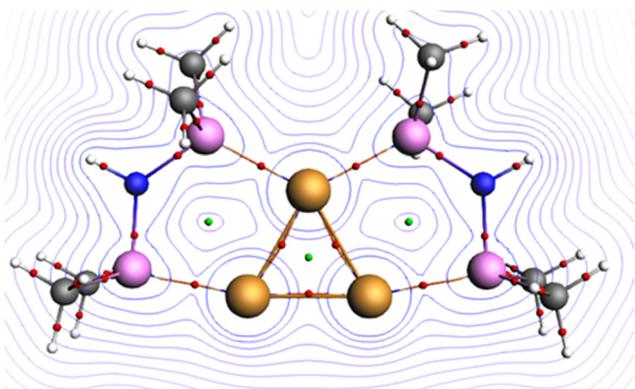


**Fig. 9** Molecular topology of nanocluster **G**.

similar in both clusters, suggesting that the effect of the third ligand is negligible (Fig. 9).

For nanocluster **H**, the data in Table 8 highlight distinct bonding characteristics in RCPs and BCPs. The RCPs exhibit low $\rho$ (0.016–0.023 a.u.) and positive $\nabla^2\rho$ (0.0317–0.0423 a.u.), indicating weak closed-shell interactions with predominantly electrostatic character. In contrast, the BCPs (Cu···H) show higher $\rho$ (0.087–0.096 a.u.) and negative $H$ (−0.0350 to −0.0436 a.u.), suggesting moderate hydrogen bonding with a mixed electrostatic–covalent nature. Notably, BCP2 ($\rho$ = 0.0963 a.u., $H$ = −0.0436 a.u.) exhibits a stronger interaction than BCP1, implying greater charge delocalization in this bonding region (Fig. 10).



**Fig. 10** Molecular topology of nanocluster **H**.

**Table 9** Topological parameters calculated for investigated nanocluster **H** BCPs and RCPs

|      | $\rho$ | $\nabla^2(\rho)$ | $G$ | $V$ | $H$ |
|------|--------|------------------|-----|-----|-----|
| RCP1 | 0.0167 | 0.0370 | 0.0093 | −0.0093 | 0.0000 |
| RCP2 | 0.0238 | 0.0317 | 0.0109 | −0.0140 | −0.0030 |
| RCP3 | 0.0176 | 0.0423 | 0.0106 | −0.0104 | 0.0001 |
| BCP1 | 0.0873 | 0.1716 | 0.0780 | −0.1130 | −0.0350 |
| BCP2 | 0.0963 | 0.1740 | 0.0871 | −0.1308 | −0.0436 |

RCP: Cu–Cu–P–N–P; BCP: Cu···H. Values are given in atomic units (a.u.).

### EDA-NOCV

The energy decomposition analysis-natural orbitals for chemical valence (EDA-NOCV) method provides a quantitative assessment of bonding interactions in metal–ligand (M–L) complexes.[79–81] This approach combines the EDA framework, originally developed by Ziegler and Rauk,[82,83] with the NOCV extension, introduced by Mitoraj and Michalak,[84,85] offering deeper insights into the nature of chemical bonding.

The EDA-NOCV method decomposes the intrinsic interaction energy ($\Delta E_{int}$) between two molecular fragments into three fundamental components:

$$\Delta E_{int} = \Delta E_{elstat} + \Delta E_{Pauli} + \Delta E_{orb}$$

where $\Delta E_{elstat}$ represent the electrostatic interaction, $\Delta E_{Pauli}$ account for Pauli repulsion and $\Delta E_{orb}$ describes orbital (covalent) interactions.

To investigate the bonding characteristics of the studied nanoclusters, the EDA-NOCV approach was applied, partitioning each system into two molecular fragments: fragment 1, consisting of the three copper atoms, and fragment 2, comprising the coordinating ligands (L), along with $BH_4$ and hydride units. The computed EDA-NOCV results are presented in Table 10. For the two series, the computed EDA-NOCV results reveal that the intrinsic interaction energies follow the trend:

$[Cu_3L_3(H)_i(BH_4)_j]^+$: **F** (−7025 kcal mol$^{-1}$) < **B** (−7084 kcal mol$^{-1}$)

$\approx$ **D** (−7089 kcal mol$^{-1}$) < **A** (−7529 kcal mol$^{-1}$)

$[Cu_3L_2(H)_i(BH_4)_j]^+$: **H** (−4662 kcal mol$^{-1}$) < **E** (−4715 kcal mol$^{-1}$)

$\approx$ **G** (−4727 kcal mol$^{-1}$) < **C** (−5160 kcal mol$^{-1}$).

**Table 10** Decomposition energy analysis of $[Cu_3L_k(H)_i(BH_4)_j]^+$ (where $k$ = 2 and 3, $i$ = 0 to 2 and $j$ = 0 and 1) nanoclusters in kcal mol$^{-1}$. PBE calculation level with the TZP basis set

|   | $\Delta E_{Pauli}$ | $\Delta E_{elstat}$ | $\Delta E_{orb}$ | $\Delta E_{int}$ |
|---|--------------------|---------------------|------------------|------------------|
| A | 23 770 | −4769 (15%) | −26 530 (85%) | −7529 |
| B | 22 509 | −4595 (16%) | −24 998 (84%) | −7084 |
| C | 16 198 | −3223 (15%) | −18 134 (85%) | −5160 |
| D | 22 416 | −4571 (15%) | −24 935 (85%) | −7089 |
| E | 15 018 | −3067 (16%) | −16 667 (84%) | −4715 |
| F | 22 307 | −4573 (16%) | −24 759 (84%) | −7025 |
| G | 14 955 | −3051 (16%) | −16 632 (84%) | −4727 |
| H | 14 844 | −3055 (16%) | −16 452 (84%) | −4662 |

This order indicates that $[\mathrm{Cu_3L_2(H)}_i\mathrm{(BH_4)}_j]^+$ fragments exhibit stronger interactions than $[\mathrm{Cu_3L_3(H)}_i\mathrm{(BH_4)}_j]^+$ analogs. The strongest bonding was observed for the $[\mathrm{Cu_3L}_k\mathrm{(H)(BH_4)}_j]^+$ nanocluster, whereas the weakest bonding was noted for $[\mathrm{Cu_3L}_k\mathrm{(H)}]^+$, where $k$ = 2 and 3.

Despite considerable Pauli repulsion, the high intrinsic interaction energies primarily arise from orbital contributions, with covalent interactions ($\Delta E_{\mathrm{orb}}$) accounting for approximately 84% of the total attractive interactions. In contrast, electrostatic contributions ($\Delta E_{\mathrm{elstat}}$) are relatively small but exhibit systematic variations, being more pronounced in **A** and **B** compared to **D** and **F**. A similar trend is observed in the $[\mathrm{Cu_3L_2(H)}_i\mathrm{(BH_4)}_j]^+$ series, where electrostatic contributions are the lowest in reference nanoclusters (**D** and **G**) and increase slightly with the addition of one or two hydride fragments. Notably, replacing a single hydride unit with a $\mathrm{BH_4}$ group results in an approximate 5% increase in electrostatic interactions. Overall, these findings underscore the dominant role of orbital interactions in stabilizing the nanoclusters, while electrostatic effects remain an important secondary factor influenced by ligand composition and substitution.

### UV-vis analysis

High-efficiency nonlinear optical (NLO) materials are widely employed in second-harmonic generation (SHG) due to their ability to facilitate frequency doubling through quadratic nonlinear interactions. For optimal performance, these materials must exhibit high optical transparency at the operational laser wavelength to minimize absorption losses and maximize nonlinear conversion efficiency. To evaluate the transparency of the investigated nanoclusters, ultraviolet-visible-near-infrared (UV-VIS-NIR) absorption spectra were computed using the TD-M06-2X/6-31+G(d)/SDD level of theory.

The results, as presented in Fig. 11, reveal that the main absorption regions of nanoclusters **D**, **F**, and **G** are confined within the ultraviolet-visible (UV-VIS) spectrum, while nanoclusters **A**, **B**, **E**, and **H** primarily absorb in the ultraviolet (UV) domain. Notably, the absorption spectrum of nanocluster C extends into the near-infrared (NIR) region, reaching up to 900 nm. From Table 11, we can note that the first electronic transitions for nanoclusters **A**, **B**, **E**, and **H** occur at 244 nm, 303 nm, 349 nm, and 348 nm, respectively. In contrast, nanoclusters **C**, **D**, **F**, and **G** exhibit red-shifted first electronic transitions, appearing at 596 nm, 644 nm, 454 nm, and 505 nm, respectively. Detailed spectral analysis reveals that all the studied nanoclusters exhibit transparency in the near-infrared (NIR) region. Notably, nanoclusters **A**, **B**, **E**, and **H** display exceptional transparency across both the NIR and visible spectral regions, a property ascribed to the absence of notable absorption features within the wavelength range of 400–700 nm.

To achieve a comprehensive understanding of the electronic transitions in the studied nanocluster, hole–electron descriptors ($D_{\mathrm{CT}}$, $\Delta\mu$, $S_{\mathrm{r}}$, $H_{\mathrm{CT}}$, and $t_{\mathrm{index}}$) were computed, and the results are summarized in Table 11, and the charge density difference (CDD) between the excited state and the ground state is
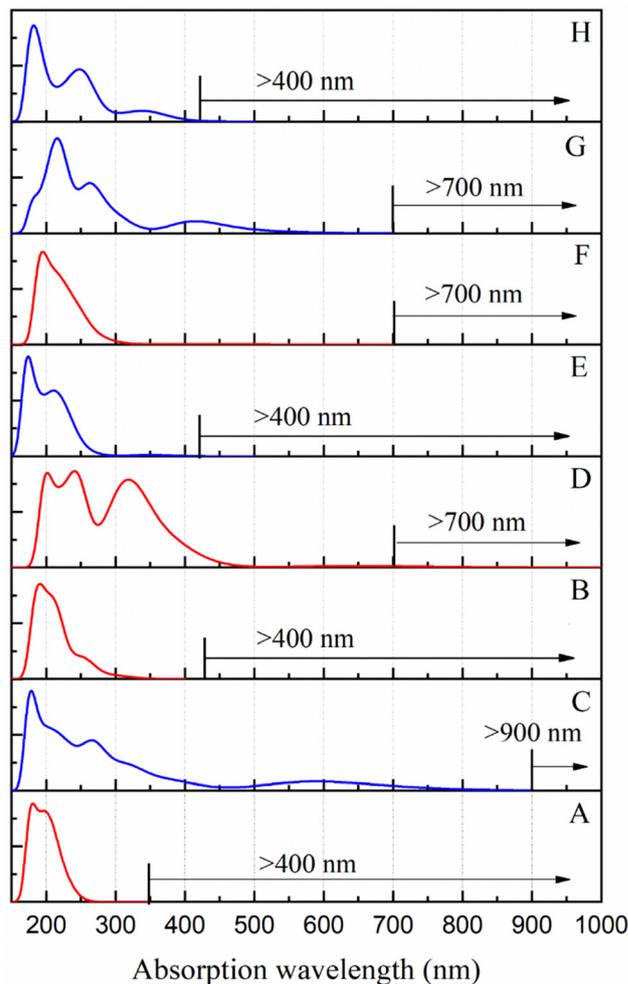


Fig. 11 The electronic spectra of **A** to **H** nanoclusters.

presented in Fig. S1 in the ESI.† The analysis indicates that the first singlet excitation (S1) of the investigated system is primarily governed by a HOMO → LUMO transition, contributing approximately 70%. For nanoclusters C, D, and G, the S1 state is mainly attributed to intramolecular charge transfer (ICT), largely confined to the copper atoms (Fig. 2). This is evidenced by the calculated overlap integrals ($S_{\mathrm{r}}$) of 0.73, 0.657, and 0.629, along with $D_{\mathrm{CT}}$ of 0.967, 0.096, and 0.794 Å. The corresponding negative $t_{\mathrm{index}}$ values suggest localized electronic excitation within these nanoclusters.

In contrast, nanoclusters **B**, **F** and **H** exhibit distinct charge transfer (CT) pathways, reflecting variations in their electronic excitation behavior. Specifically, in **B**, the S1 state is governed by hydride-to-ligand charge transfer (HLCT) and metal-to-ligand CT (MLCT). In **F**, the excitation corresponds to ligand-to-hydride CT (LHCT), while in **H**, it is primarily associated with ligand-to-metal CT (LMCT). These transitions exhibit a positive $t_{\mathrm{index}}$, with overlap integrals ($S_{\mathrm{r}}$) of 0.518, 0.459, and 0.507, and the corresponding $D_{\mathrm{CT}}$ of 1.628, 2.550, and 2.511 Å, respectively. Furthermore, nanocluster **F** exhibits the largest dipole moment variation ($\Delta\mu$ = 12.239 Debye), surpassing **H** (12.061 Debye) and

**Table 11** Excitation wavelength ($\lambda_{0 \to n}$, nm) and energy ($E$, eV) and oscillator strengths ($f$), variation dipole moment ($\Delta\mu$, Debye), overlap ($S_r$), $D_{CT}$, index $H$ and $t_{index}$ (Å) associated with the $S_0 \to S_n$ transitions, as calculated at M06-2X/SDD/6-31+G(d) of the studied complexes **A** to **H**

| | Sn | $\Delta\lambda_{0 \to n}$ | $E_{0 \to n}$ | $f$ | $S_r$ | $D_{CT}$ | $\Delta\mu$ | $H$ | $t_{index}$ | Transition |
|---|---|---|---|---|---|---|---|---|---|---|
| A | S1 | 244 | 5.072 | 0.001 | 0.562 | 0.615 | 2.957 | 3.373 | −0.658 | H → L+3 (42%); H → L (20%) |
| | S8 | 214 | 5.776 | 0.159 | 0.612 | 0.440 | 2.105 | 3.394 | −1.398 | H → L+5 (32%); H → L+7 (22%) |
| | S10 | 214 | 5.781 | 0.165 | 0.610 | 0.537 | 2.562 | 3.351 | −1.292 | H → L+6 (34%); H → L+8 (24%) |
| B | S1 | 303 | 4.086 | 0.032 | 0.518 | 1.628 | 7.859 | 2.764 | 0.033 | H → L (56%); H → L+1 (20%) |
| | S4 | 354 | 4.867 | 0.065 | 0.562 | 0.208 | 1.001 | 3.376 | −1.770 | H → L+2 (16%); H → L+ (32%) |
| | S5 | 251 | 4.939 | 0.065 | 0.543 | 0.990 | 4.752 | 3.436 | −1.042 | H → L+1 (27%); H−2 → L (17%) |
| | S19 | 219 | 5.656 | 0.173 | 0.582 | 0.311 | 1.493 | 3.808 | −1.555 | H → L+10 (12%); H → L+3 (8%) |
| | S27 | 207 | 5.970 | 0.132 | 0.583 | 0.374 | 1.787 | 3.963 | −1.453 | H → L+3 (10%); H → L+4 (8%) |
| C | S1 | 596 | 2.079 | 0.095 | 0.730 | 0.967 | 4.626 | 2.749 | −0.666 | H → L (80%); H → L+3 (8%) |
| | S2 | 513 | 2.418 | 0.011 | 0.593 | 1.477 | 7.069 | 2.896 | −0.007 | H → L+1 (88%); H → L (10%) |
| | S3 | 396 | 3.134 | 0.034 | 0.679 | 0.996 | 4.760 | 3.091 | −0.810 | H → L+3 (62%); H → L+2 (14%) |
| | S4 | 375 | 3.307 | 0.046 | 0.657 | 1.178 | 5.632 | 3.124 | −0.644 | H → L+4 (74%); H → L+5 (8%) |
| | S5 | 331 | 3.743 | 0.052 | 0.417 | 3.274 | 15.572 | 3.354 | 1.198 | H → L+2 (38%); H → L+6 (36%) |
| | S10 | 276 | 4.500 | 0.147 | 0.527 | 1.715 | 8.146 | 3.947 | −0.550 | H → L+10 (44%); H → L+9 (28%) |
| D | S1 | 644 | 1.926 | 0.009 | 0.657 | 0.096 | 0.463 | 2.858 | −1.335 | H → L (98%) |
| | S2 | 388 | 3.198 | 0.061 | 0.560 | 0.739 | 3.548 | 3.120 | −1.071 | H → L+4 (88%) |
| | S6 | 340 | 3.650 | 0.097 | 0.366 | 0.963 | 4.572 | 4.094 | −1.684 | H → L+2 (70%); H → L+6 (8%) |
| | S9 | 320 | 3.878 | 0.138 | 0.532 | 0.500 | 2.383 | 3.733 | −1.934 | H → L+10 (28%); H → L+9 (20%) |
| | S12 | 296 | 4.1851 | 0.1101 | 0.448 | 1.415 | 6.768 | 4.154 | −1.358 | H → L+6 (44%); H → L+9 (26%) |
| E | S1 | 349 | 3.55 | 0.012 | 0.519 | 0.686 | 3.288 | 2.579 | −0.887 | H → L (92%) |
| | S2 | 277 | 4.476 | 0.003 | 0.518 | 0.488 | 2.367 | 2.721 | −1.261 | H → L+1 (76%); H → L+2 (8%) |
| | S6 | 236 | 5.247 | 0.148 | 0.624 | 1.081 | 5.169 | 2.923 | −0.683 | H → L+5 (28%); H → L+3 (20%) |
| | S8 | 226 | 5.489 | 0.116 | 0.641 | 0.384 | 1.834 | 3.024 | −1.533 | H → L+4 (16%); H → L+5 (14%) |
| | S14 | 211 | 5.888 | 0.069 | 0.453 | 0.898 | 4.285 | 2.738 | −0.630 | H → L+7 (54%) |
| F | S1 | 454 | 2.732 | 0.002 | 0.459 | 2.550 | 12.239 | 2.726 | 0.870 | H → L (91%) |
| | S2 | 347 | 3.313 | 0.002 | 0.469 | 1.636 | 7.867 | 2.872 | −0.147 | H → L+1 (46%); H → L+2 (42%) |
| | S6 | 288 | 4.310 | 0.014 | 0.475 | 2.551 | 12.242 | 3.262 | 0.457 | H → L+4 (56%); H → L+5 (16%) |
| | S7 | 281 | 4.419 | 0.02 | 0.563 | 1.643 | 7.883 | 3.293 | −0.484 | H−4 → L (22%); H−2 → L+1 (20%) |
| | S10 | 260 | 4.776 | 0.035 | 0.456 | 3.271 | 15.640 | 3.709 | 0.800 | H → L+4 (12%); H → L+1 (10%) |
| | S12 | 252 | 4.920 | 0.05 | 0.392 | 4.224 | 20.205 | 3.397 | 2.055 | H → L+7 (24%); H → L+3 (18%) |
| G | S1 | 505 | 2.454 | 0.017 | 0.629 | 0.794 | 3.811 | 2.701 | −0.702 | H → L (98%) |
| | S2 | 413 | 2.999 | 0.116 | 0.675 | 0.639 | 3.059 | 2.799 | −1.091 | H → L+1 (96%) |
| | S4 | 308 | 4.030 | 0.086 | 0.573 | 0.156 | 0.745 | 3.122 | −1.602 | H → L+5 (82%) |
| | S9 | 280 | 4.434 | 0.102 | 0.697 | 0.209 | 1.002 | 3.124 | −1.948 | H → L+2 (34%); H → L+9 (34%) |
| | S11 | 262 | 4.723 | 0.362 | 0.648 | 0.672 | 3.224 | 3.480 | −1.352 | H → L+9 (38%); H → L+2 (20%) |
| H | S1 | 348 | 3.563 | 0.068 | 0.507 | 2.511 | 12.061 | 2.658 | 0.797 | H → L (92%) |
| | S2 | 339 | 3.658 | 0.008 | 0.471 | 2.195 | 10.536 | 2.602 | 0.575 | H → L (90%) |
| | S3 | 311 | 3.988 | 0.024 | 0.401 | 2.890 | 13.881 | 2.550 | 1.339 | H → L+2 (90%) |
| | S6 | 265 | 4.670 | 0.127 | 0.565 | 2.357 | 11.317 | 2.801 | 0.551 | H → L+3 (32%); H → L+5 (20%) |
| | S9 | 251 | 4.941 | 0.105 | 0.533 | 2.003 | 9.620 | 2.746 | 0.307 | H → L+3 (54%); H → L+2 (10%) |
| | S11 | 242 | 5.120 | 0.105 | 0.662 | 1.076 | 5.168 | 3.106 | −0.954 | H → L+3 (58%); H → L+4 (12%) |

**B** (7.859 Debye). Meanwhile, nanocluster **A** demonstrates a mixed CT character, involving both LLCT and MLCT, with associated descriptors $S_r$ = 0.562 and $D_{CT}$ = 0.615 Å.

In the case of reference nanoclusters **D** and **G**, the hole–electron distributions corresponding to the S6 and S2 electronic transitions, occurring at 340 nm and 413 nm, respectively, are predominantly localized on the copper centers and surrounding molecular fragments. The computed centroid separation between the hole and electron distributions remains relatively small, with $D_{CT}$ values of 0.963 and 0.639 Å, respectively. Furthermore, these transitions exhibit moderate dipole moment variations ($\Delta\mu$ = 4.572 and 3.059 Debye), indicative of localized electronic excitation (Fig. S1, ESI†). For nanoclusters **A** and **C**, the S8 and S10 excitations are mainly concentrated on

the BH$_4$ group, hydride unit, and copper atoms. The corresponding centroid separations are computed as 0.440 Å for **A** and 1.715 Å for **C**. Notably, nanocluster **C** exhibits a significantly larger dipole moment variation ($\Delta\mu$ = 8.146 Debye) compared to **A** ($\Delta\mu$ = 2.105 Debye), suggesting a stronger polarization effect in the excited state.

Regarding nanocluster **F**, the S2 and S6 excitations, located at 347 nm and 288 nm, respectively, exhibit considerable charge separation, as reflected by centroid distances of $D_{CT}$ = 1.636 and 2.551 Å, respectively. Additionally, these transitions are characterized by significant dipole moment variations ($\Delta\mu$ = 7.867, 12.242 Debye), suggesting enhanced charge redistribution upon excitation. The computed overlap integrals ($S_r$ = 0.469 and 0.475), along with the hole delocalization indices ($H$ = 2.872 and 3.262),

further support the presence of extended charge transfer. A similar trend is observed for nanocluster **H**, where the S3, S6, and S9 transitions at 311, 265, and 251 nm, respectively, exhibit notable centroid separations (2 Å < $D_{CT}$ < 2.9 Å). The corresponding oscillator strengths ($f$ = 0.024, 0.127, and 0.105) indicate varying transition intensities. Additionally, these excitations display substantial dipole moment variations ($\Delta\mu$ = 13.881, 11.31 and 9.620 Debye), signifying pronounced charge redistribution. The hole–electron densities in these transitions are predominantly localized on the copper centers and ligand framework, reinforcing their involvement in the electronic excitation process.

## Polarizability and dipole moment

The polarizability ($\alpha$) of a matter represents the extent to which its electron cloud can be distorted under the influence of an external electric field, whereas the anisotropic polarizability ($\Delta\alpha$) quantifies the variation in this polarizability as a function of direction within the matter framework.[86] The calculated isotropic polarizability and its anisotropy and dipole moment of the title cluster are listed in Table 12.

From our results we can note that nanoclusters **A** and **B** exhibit strikingly similar values for dipole moment, polarizability, and polarizability anisotropy (1.924 D, 376 a.u., and 90 a.u., respectively). This observation suggests that the substitution of the $BH_4$ group with a hydride ligand induces negligible changes in these electronic parameters, reflecting minimal structural or electronic perturbations associated with this modification. Likewise, nanocluster **F** demonstrates comparable polarizability and anisotropy values (368 and 92 a.u., respectively). However, the removal of either the hydride or the $BH_4$ group from **A** and **B** results in a substantial increase in the dipole moment of **F** (11.511 D), highlighting a dramatic redistribution of electronic density upon this structural change. For nanocluster **D**, the elimination of both the hydride and $BH_4$ ligands yields the highest polarizability ($\alpha$ = 403 a.u.) and polarizability anisotropy ($\Delta\alpha$ = 148 a.u.), indicative of a highly flexible electron cloud and substantial structural anisotropy. Despite these characteristics, the low dipole moment ($\mu$ = 0.965 D) suggests a nearly symmetric charge distribution, highlighting a minimal degree of charge separation within the cluster.

On the other hand, compounds **E** and **H** have the lowest polarizability ($\alpha$ = 264 and 266, respectively), with correspondingly low anisotropic polarizability ($\Delta\alpha$ = 72 and 62 a.u., respectively) but substantial dipole moments ($\mu$ = 4.694 and

9.789 Debye, respectively), indicating compact structures with localized polarization. Moderate values for $\alpha$ and $\Delta\alpha$, such as those of compound **C** ($\alpha$ = 332 a.u., $\Delta\alpha$ = 87 a.u., $\mu$ = 6.130 Debye), reflect balanced electronic distributions with considerable permanent dipole moments due to specific polar bonds or functional groups. A comparison of nanocluster **G** with nanoclusters **C**, **E**, and **H** reveals that the removal of hydride and $BH_4$ ligands results in a comparable polarizability (285 a.u.) and the highest polarizability anisotropy (104 a.u.) observed among the studied $[Cu_3L_2(H)_i(BH_4)_j]^+$ systems. This outcome underscores the significant influence of ligand removal on enhancing anisotropic electronic properties while maintaining similar overall polarizability.

The results presented in Table 12 and Fig. 12 indicate that the polarizability of the nanocluster $[Cu_3L_3(H)_i(BH_4)_j]^+$ is higher than that of its counterpart, $[Cu_3L_2(H)_i(BH_4)_j]^+$ ($i$ = 0, 1 and 2 and $j$ = 0 or 1). Among the studied compounds, **D**, **F**, **A** and **B** exhibit the highest polarizability values. These findings suggest that the presence of three ligands (L) compared to two ligands in a structure leads to increased polarizability. Additionally, the calculated anisotropic polarizability ($\Delta\alpha$), ranging from 62 to 148 a.u., appears to be moderately influenced by the L, $BH_4$ ligand and hydride substituents. Moreover, the effect of the incident wavelength ($\lambda$ = 1340 and 1064 nm) on polarizability and anisotropic polarizability is determined to be negligible, indicating minimal wavelength dependency in these optical properties.

## Second order nonlinear optical (NLO) response

For the investigated nanoclusters, the static first hyperpolarizability ($\beta_{tot}^0$) and hyper-Rayleigh scattering hyperpolarizability ($\beta_{HRS}^0$) were computed at the same theoretical level, and the corresponding results are presented in Fig. 13.

The ligand environment plays a critical role in determining the first hyperpolarizability ($\beta_{tot}^0$) and HRS ($\beta_{HRS}^0$) of nanoclusters, as it directly influences the electronic distribution, symmetry and polarizability and its anisotropy of the system. In the studied nanoclusters (**A** to **H**), the ligand type, number, and arrangement variation significantly modulate their nonlinear optical properties. The static first hyperpolarizability of the title nanocluster exhibits the following overall ordering: $\beta_{tot}^0$: **E** < **A** < **B** < **D** < **G** < **F** < **C** < **H** ($\beta_{HRS}^0$: **E** < **A** < **B** < **G** < **F** < **D** < **C** < **H**). From a more detailed analysis, the second-order NLO response of the $Cu_3L_3H_i(BH_4)_j$ series was found to display the following ordering: $\beta_{tot}^0$: **A** < **B** < **D** < **F** and $\beta_{HRS}^0$: **A** < **B** < **F** < **D**. The first hyperpolarizability is relatively small in nanocluster **A** but increases notably upon substitution of the $BH_4$ group with a hydride ligand in nanocluster **B** or the removal of both $BH_4$ and hydride ligands in nanocluster **D**. Notably, nanocluster **F**, containing a single hydride ligand, exhibits the highest first hyperpolarizability among the systems studied. For instance, the $\beta_{tot}^0$ value of nanocluster **F** is approximately 5 times greater than that of nanocluster **D** (Fig. 13).

Within the $[Cu_3L_2H_i(BH_4)_j]^+$ series, nanocluster **H**, characterized by the presence of a single hydride ligand, exhibits the

**Table 12** Calculated polarizability ($\alpha$, a.u.), polarizability anisotropy ($\Delta\alpha$, a.u.) and dipole moment ($\mu$, Debye)

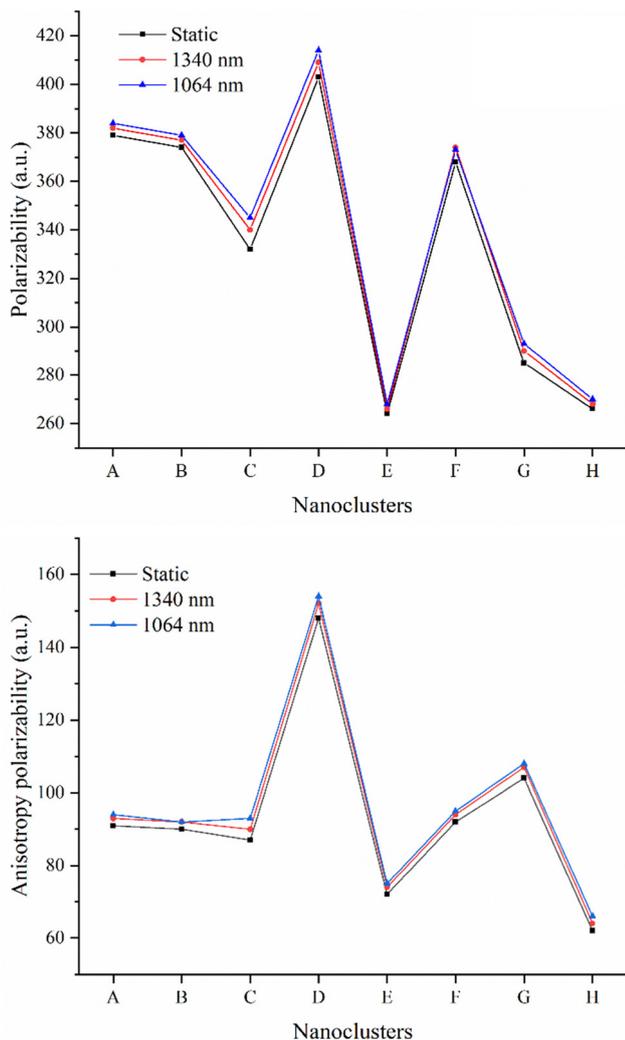|   | $\alpha$ (a.u.) | $\Delta\alpha$ (a.u.) | $\mu$ (Debye) |
|---|---|---|---|
| **A** | 379 | 91 | 1.954 |
| **B** | 374 | 90 | 1.894 |
| **C** | 332 | 87 | 6.130 |
| **D** | 403 | 148 | 0.965 |
| **E** | 264 | 72 | 4.694 |
| **F** | 368 | 92 | 11.511 |
| **G** | 285 | 104 | 3.563 |
| **H** | 266 | 62 | 9.789 |

Fig. 12 Variation of polarizability and anisotropic polarizability in the static and dynamic regime of nanoclusters **A** to **H**.
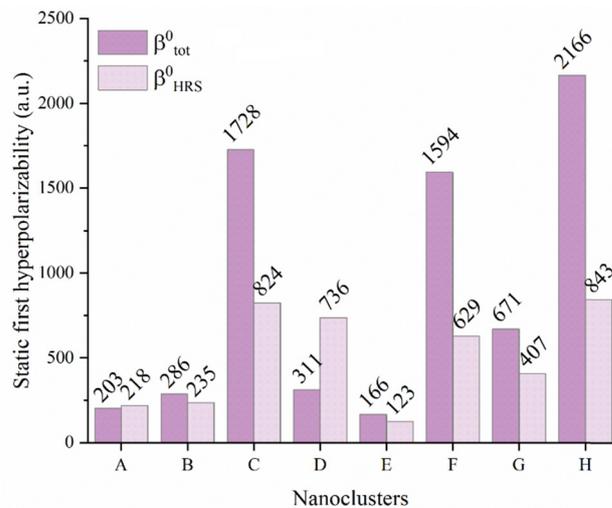


Fig. 13 Variation in static first hyperpolarizability ($\beta^0_{tot}$) and hyper–Rayleigh scattering hyperpolarizability ($\beta^0_{HRS}$) for nanoclusters **A** to **H**.

highest second-order NLO response. This response is diminished in nanocluster **C** with the incorporation of a $BH_4$ ligand and further reduced in nanocluster **G** upon the removal of the hydride group. Nanocluster **E**, which contains two hydride ligands, demonstrates the lowest second-order NLO response in the series. For example, the $\beta^0_{tot}$ [$\beta^0_{HRS}$] value of **H** is 2166 a.u. [843 a.u.], which is 13 [7] times larger than that of **E**. The ordering of the $\beta^0_{tot}$ and $\beta^0_{HRS}$ value for the nanoclusters $Cu_3L_2$-$H_i(BH_4)_j$ is **E** < **G** < **C** < **H** (Fig. 13). These results underscore the pivotal role of ligand composition and symmetry in determining the NLO performance of $[Cu_3L_kH_i(BH_4)_j]^+$ hydride nanoclusters.

For example, nanocluster **G** exhibits a higher static first hyperpolarizability ($\beta^0_{tot}$ = 671 a.u.) compared to **D** ($\beta^0_{tot}$ = 311 a.u.). This can be attributed to **G**'s larger dipole moment (3.563 D), which enhances its charge redistribution under an applied field. However, **D** demonstrates a greater $\beta^0_{HRS}$ value (736 a.u.) compared to **G** (407 a.u.), despite its lower $\beta^0_{tot}$. This discrepancy arises due to **D** having a higher polarizability

anisotropy (148 a.u.) compared to **G** (104 a.u.). The larger anisotropy in **D** reflects a more directional electronic response, amplifying the hyperpolarizability contribution in processes associated with second-order scattering, such as hyper-Rayleigh scattering. Therefore, while **G** benefits from stronger overall charge redistribution ($\beta^0_{tot}$), **D**'s enhanced anisotropic polarization drives its superior $\beta^\infty_{HRS}$. A similar trend is observed for nanoclusters **D** and **F**, where **F** exhibits a significantly higher static first hyperpolarizability ($\beta^0_{tot}$ = 1594 a.u.) compared to **D** (311 a.u.), primarily due to its substantial dipole moment ($\mu(\mathbf{F})$ = 11.511 D). Conversely, nanocluster **D** displays a $\beta^0_{HRS}$ value that is 17% larger than that of **F**, attributed to its greater polarizability anisotropy.

On the other hand, nanocluster **C** exhibits a higher first hyperpolarizability than nanocluster **A**, a distinction that can be attributed to the characteristics of the Cu···H–B bonds (BCP′). According to QTAIM analysis, the BCP′ in nanocluster **A** is stronger and associated with a higher potential energy ($V$) compared to the corresponding bond in nanocluster **C**. This indicates that the electrons within the Cu···H–B bonds in nanocluster **A** are more tightly localized. Conversely, in nanocluster **C**, the Cu···H–B bonds exhibit greater electron delocalization and mobility (Tables 2 and 4). The increased electron delocalization observed in nanocluster **C** contributes significantly to its superior first hyperpolarizability compared to nanocluster **A**.

In addition, the first hyperpolarizability ($\beta^0_{HRS}$ and $\beta^0_t$) of nanocluster **B** is marginally higher than that of nanocluster **E**, with a difference of approximately 20%. This variation can be attributed to the potential energy of the Cu···H bond (BCPs) in the two systems. In nanocluster **B**, the potential energy ranges from −0.09 to −0.05 a.u., whereas in nanocluster **E**, it spans from −0.11 to −0.07 a.u. (Tables 3 and 6). The more negative potential energy values observed in nanocluster **E** suggest greater electron localization compared to **B**, where the potential energy is less negative. This increased electron localization in **E**

reduces its capacity for charge redistribution under an applied electric field, thereby slightly lowering its first hyperpolarizability relative to nanocluster **B**.

On the other hand, the higher first hyperpolarizability of nanocluster **H** compared to **F** can be attributed to the kinetic energy within the Cu–H bonds, which is greater in **H** (Tables 7 and 9). This indicates that electrons in Cu–H bonds are less localized in **H** than in **F**. Notably, the presence of a single hydride atom linking two copper atoms has a more pronounced impact on the electronic properties and first hyperpolarizability than a hydride coordinated to three copper atoms (Fig. 8 and 10).

Based on this analysis, it can be concluded that the structural topology of the title nanocluster, along with the spatial distribution of ligands around the copper atoms, exerts a more significant influence on the modulation and prediction of first hyperpolarizability than the number or chemical nature of the ligands within the system.

### Frequency-dependent first hyperpolarizability

In this study, we analysed the frequency-dependent first hyperpolarizability to evaluate the potential applications of the nanoclusters with the highest first hyperpolarizability values within each series. These computations were carried out at wavelengths of 1064 nm (0.04282 a.u.) and 1340 nm (0.0340 a.u.). The selected wavelengths are particularly relevant to the operation of Nd:YAG lasers, which commonly emit at longer wavelengths in the near-infrared region.[87] The values of the electro-optical Pockels effect ($\beta^{\omega}_{\text{EOPE}}$), second harmonic generation ($\beta^{\omega}_{\text{SHG}}$) and dynamic hyper-Rayleigh scattering ($\beta^{\omega}_{\text{HRS}}$) first hyperpolarizability are listed in Table 13.

The calculated values for the electro-optical Pockels effect ($\beta(-\omega; \omega, 0)$) for the highest-performing NLO nanoclusters **H**, **F**, **C**, and **G** at 1340 nm are 2370, 1708, 1401, and 1032 a.u., respectively. In contrast, nanoclusters **E**, **A**, **B**, and **D** exhibit significantly lower EOPE values at 1340 nm, with $\beta(-\omega; \omega, 0)$ values of 175, 189, 287, and 414 a.u., respectively. Interestingly, nanoclusters **D**, **E**, **G**, and **H** demonstrate higher $\beta(-\omega; \omega, 0)$ values at 1340 nm compared to their corresponding $\beta^0_{\text{tot}}$. At 1064 nm, the $\beta(-\omega; \omega, 0)$ values for the nanoclusters are generally higher than those observed at 1340 nm, except for nanocluster **C**, which shows a lower value of 1322 a.u.

These results indicate that the electro-optical Pockels effect is more sensitive to shorter wavelengths.

The second harmonic generation (SHG) hyperpolarizability values, $\beta(-2\omega; \omega, \omega)$, for the highest-performing NLO nanoclusters **D**, **C**, and **G** at 1340 nm are 1631, 4199, and 1492 a.u., respectively. Nanoclusters **C**, **G**, and **H** exhibit significantly greater sensitivity at 1064 nm, with corresponding SHG values of 7776, 2627, and 3543 a.u., respectively, demonstrating a marked increase compared to their static $\beta^0_{\text{tot}}$ values. At 1064 nm, the hyper-Rayleigh scattering first hyperpolarizability values ($\beta^{\lambda}_{\text{HRS}}$) for nanoclusters **C**, **H**, **G**, and **F** are 7776, 3543, 2627, and 2253 a.u., respectively. Furthermore, the $\beta^{\lambda}_{\text{HRS}}$ values at 1340 nm are consistently lower than their corresponding values at 1064 nm.

It is evident that both $\beta^{\lambda}_{\text{HRS}}$ and $\beta^{\lambda}_{\text{SHG}}$ responses are generally more pronounced at 1064 nm compared to 1340 nm, with the exception of nanocluster **D**, which deviates from this trend. Furthermore, the first hyperpolarizability in the dynamic regime is significantly larger than in the static regime. For instance, the $\beta^{\lambda}_{\text{HRS}}$ and $\beta^{\lambda}_{\text{SHG}}$ responses for nanocluster **C** at 1064 nm are approximately four times greater than those in the static regime. Similarly, for nanocluster **G**, the $\beta^{\lambda}_{\text{HRS}}$ and $\beta^{\lambda}_{\text{SHG}}$ responses at 1340 nm and 1064 nm are approximately two and three times, respectively, larger than their static values. These results emphasize that $\beta^{\lambda}_{\text{HRS}}$ and $\beta^{\lambda}_{\text{SHG}}$ responses are more sensitive to shorter wavelengths, displaying enhanced values at smaller wavelengths. However, the frequency-dependent effect on the electro-optical Pockels effect (EOPE) is comparatively weaker than on SHG, with the notable exception of nanocluster **D** at 1064 nm, where the EOPE response is relatively pronounced.

To further investigate the factors influencing the first hyperpolarizability of the studied nanoclusters, polarization scans of the hyper-Rayleigh scattering (HRS) intensity ($I^{2\omega}_{\Psi V}$) were conducted. The relationship between $I^{2\omega}_{\Psi V}$ and the polarization angle $\psi$ was calculated and plotted (Fig. 14), along with the corresponding depolarization ratio (DR) values. The results reveal that the DR values are sensitive to ligand composition and follow the descending order: **H** > **F** > **G** > **C** > **E** ≈ **B** > **A** ≈ **D**. Notably, nanoclusters **F** and **H** exhibit predominant dipolar symmetry in their NLO responses, with DR values of 5.971 and 6.366, respectively. In contrast, nanoclusters **B**, **E**, **G**, and **C** are classified as octupolar systems, with DR values of 1.943, 2.060, 2.434, and 3.463, respectively. For nanoclusters **A** and **D**, the DR values are 1.736 and 1.546, respectively, as shown in Fig. 3. These values, being close to 1.5, are indicative of typical octupolar symmetry.

On the other hand, the results reveal that the depolarization ratio (DR) exhibits slight sensitivity to the wavelength of the incident light. Specifically, DR values follow the descending order: DR ($\lambda = 1064$ nm) > DR ($\lambda = 1340$ nm) > DR ($\lambda = \infty$). Additionally, from the data presented in Fig. 3, nanocluster **D** displays a notably low DR value (DR = 0.999, less than the threshold of 1.5). This low DR suggests that nanocluster **D** is near resonance at $\lambda = 1340$ nm, indicating enhanced nonlinear optical interactions under this specific wavelength.

**Table 13** Calculated electro-optical Pockels effect ($\beta^{\omega}_{\text{EOPE}}$), second harmonic generation ($\beta^{\omega}_{\text{SHG}}$) and dynamic hyper-Rayleigh scattering ($\beta^{\omega}_{\text{HRS}}$) first hyperpolarizability in a.u. for nanoclusters **A** to **H** in the dynamic regime

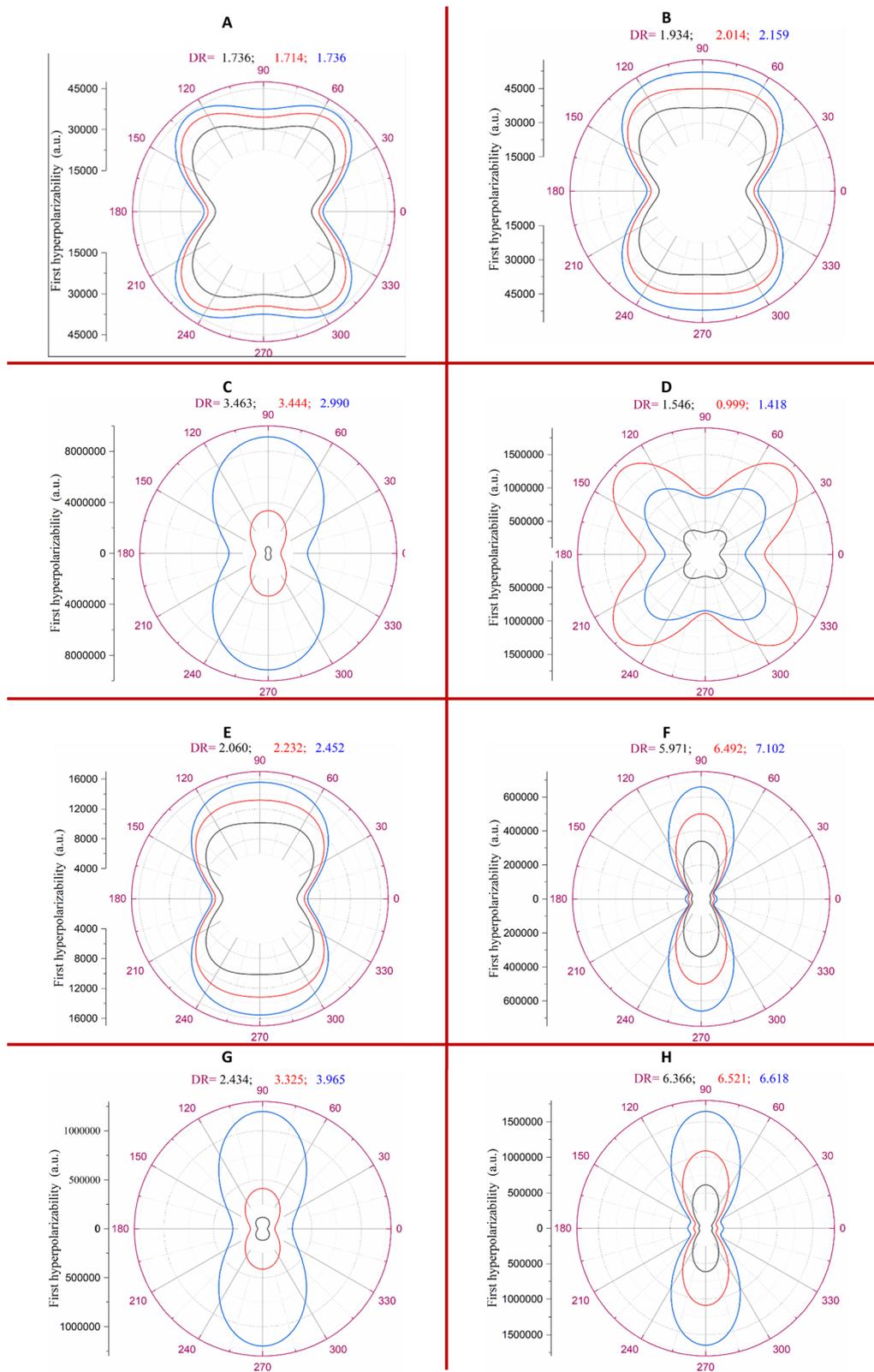|   | $\omega = 0.0340$ a.u. ($\lambda = 1340$ nm) | | | $\omega = 0.04282$ a.u. ($\lambda = 1064$ nm) | | |
|---|---|---|---|---|---|---|
|   | $\beta^{\omega}_{\text{EOPE}}$ | $\beta^{\omega}_{\text{SHG}}$ | $\beta^{\omega}_{\text{HRS}}$ | $\beta^{\omega}_{\text{EOPE}}$ | $\beta^{\omega}_{\text{SHG}}$ | $\beta^{\omega}_{\text{HRS}}$ |
| **A** | 189 | 207 | 234 | 194 | 225 | 243 |
| **B** | 287 | 339 | 259 | 301 | 400 | 276 |
| **C** | 1401 | 4199 | 2083 | 1322 | 7776 | 3492 |
| **D** | 414 | 1631 | 1332 | 478 | 381 | 1202 |
| **E** | 175 | 204 | 138 | 183 | 239 | 148 |
| **F** | 1708 | 1952 | 760 | 1773 | 2253 | 868 |
| **G** | 1032 | 1492 | 733 | 1132 | 2627 | 1225 |
| **H** | 2370 | 2884 | 1121 | 2502 | 3543 | 1377 |

**Fig. 14** Relationship between $I_{\Psi V}^{2w}$ and polarization angle $\Psi$ of nanoclusters **A** to **H** (black: static; red: $\lambda = 1340$ nm; blue: $\lambda = 1064$ nm).

To gain deeper insight into the variations in first hyperpolarizability values and their primary determining factors, we employed the conventional two-level model approach proposed by Oudar *et al.*[88,89] The mathematical formulation

of this model is expressed as follows:

$$\beta_0 \propto \frac{f \times \Delta\mu}{\Delta E^3}$$

where $\Delta\mu$ represents the excited state dipole moment, $f$ denotes the oscillator strength, and $\Delta E$ is the energy of the electronic transition. This relationship highlights that a lower excitation energy $\Delta E$, a greater dipole moment ($\Delta\mu$), and a higher oscillator strength ($f$) contribute to maximizing the first hyperpolarizability of the compound.

It is well established that molecular nonlinear optical properties calculated *via* the sum-over-states (SOS) method strongly depend on the number of excited states considered. In this study, 90 excited states were calculated at the M06-2X/6-31+G(d)/SDD level of theory. The results presented in the ESI† (Fig. S2a and b) show that, in general, 90 excited states are sufficient for converging the $\beta_{SOS}$ value. On the other hand, the two-level analysis discloses that the excited state S8 predominantly influences the hyperpolarizability of nanocluster **A**. Furthermore, critical excited states S1, S6, and S2 exhibit the highest hyperpolarizability in nanoclusters **C**, **E**, and **G**, respectively. These electronic transitions are attributable to ICT processes, as depicted in Fig. 15. In the case of hydride nanoclusters **B**, **D**, **F**, and **H**, the principal contributions to their hyperpolarizability values are attributed to the S5, S6, S7, and S6 excited states, respectively. For both series $[Cu_3L_3(H)_i-(BH_4)_j]^+$ and $[Cu_3L_2(H)_i(BH_4)_j]^+$, our results reveal a direct correlation between the dipole moment variation ($\Delta\mu$) of crucial excited states and the first hyperpolarizability of the title nanoclusters, except for **E**. Notably, nanoclusters **H** and **F** exhibit the highest dipole moment variations of 11.317 and 7.883 Debye, respectively. These excitations are characterized

by charge transfer from the hydride, copper, and ligand to the second ligand, with a $D_{index}$ of approximately 2.4 Å.

Furthermore, our results indicate that a single hydride unit enhances the dipole moment variation ($\Delta\mu$) of crucial excited states more effectively than two hydride units or a hydride and $BH_4$ fragment. These results are consistent with our previous study, which highlighted the significant role of a single hydride in modulating the electronic topology and second-order NLO responses.

### Third order nonlinear optical (NLO) response

To explore the third-order nonlinear optical properties of the studied nanoclusters, we evaluated the electric-field-induced second harmonic generation (EFISHG) $\gamma(-2\omega; \omega, \omega, 0)$, the dc-Kerr effect $\gamma(-\omega; \omega, 0, 0)$, and the quadratic nonlinear refractive index ($n_2$), and the results of the calculation are listed in Table 14. Similar to the dynamic first hyperpolarizability analysis, the frequency dispersion behavior was examined at the same wavelengths of 1340 nm (0.034 a.u.) and 1064 nm (0.04282 a.u.).

Based on our results, it is observed that the second hyperpolarizability $\gamma(0; 0, 0, 0)$ does not follow the same trend as the static first hyperpolarizability. Nanocluster **C** exhibits an exceptionally high static second hyperpolarizability ($\gamma(0; 0, 0, 0) = 173.48 \times 10^4$ a.u.) compared to the other nanoclusters. Moderate $\gamma(0; 0, 0, 0)$ values are observed for nanoclusters **D** ($17.04 \times 10^4$ a.u.), **G** ($10.182 \times 10^4$ a.u.) and **F** ($9.22 \times 10^4$ a.u.). Nanocluster **H** displays a static second hyperpolarizability of $7.469 \times 10^4$ a.u., which is comparable to that of nanocluster **A** ($7.394 \times 10^4$ a.u.). The lowest static hyperpolarizability value is found for nanocluster **E** ($5.688 \times 10^4$ a.u.).



| A (S10) | B (S5) | C (S3) | D (S6) |
| 5.781 eV, 2.562 D | 4.939 eV, 3.436 D | 3. 134 eV, 4.760 D | 3.650 eV, 4.572 D |

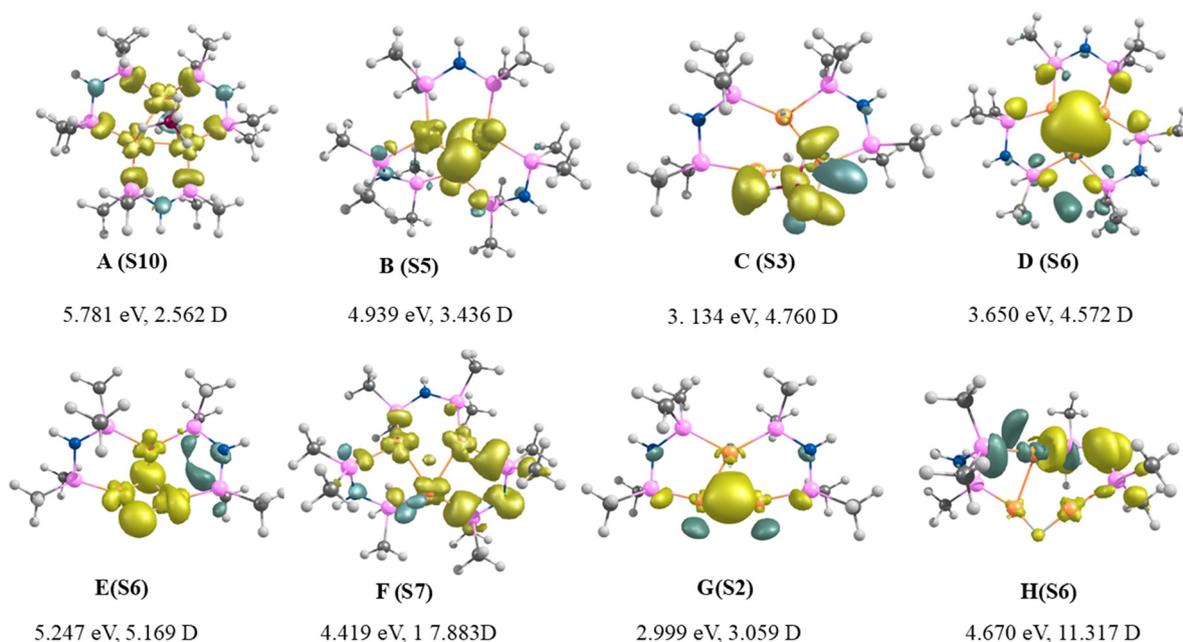| E(S6) | F (S7) | G(S2) | H(S6) |
| 5.247 eV, 5.169 D | 4.419 eV, 1 7.883D | 2.999 eV, 3.059 D | 4.670 eV, 11.317 D |

**Fig. 15** CDD for the crucial excited state of nanoclusters **A** to **H**. CDD was calculated as the difference between the corresponding excited state and the ground state of the considered system using the M06-2X/6-31+G(d)/SDD level of theory.

This journal is © The Royal Society of Chemistry and the Centre National de la Recherche Scientifique 2025

**Table 14** Estimated values $\gamma(0; 0, 0, 0)$, $\gamma(-\omega; \omega, 0, 0)$ and $\gamma(-2\omega; \omega, \omega, 0)$, and $n_2$ (cm$^2$ W$^{-1}$) values in a.u. for nanoclusters **A** to **H**

| $\omega$ | $\gamma(0; 0, 0, 0)$ $\times 10^4$ a.u. | $\omega = 0.034$ a.u. | | $\omega = 0.04282$ a.u. | | $\omega = 0.034$ a.u. | $\omega = 0.04282$ a.u. |
|---|---|---|---|---|---|---|---|
| | | $\gamma(-\omega; \omega, 0, 0)$ $\times 10^4$ a.u. | $\gamma(-2\omega; \omega, \omega, 0)$ $\times 10^4$ a.u. | $\gamma(-\omega; \omega, 0, 0)$ $\times 10^4$ a.u. | $\gamma(-2\omega; \omega, \omega, 0)$ $\times 10^4$ a.u. | $n_2 \times 10^{-18}$ cm$^2$ W$^{-1}$ | $n_2 \times 10^{-18}$ cm$^2$ W$^{-1}$ |
| A | 7.394 | 7.635 | 8.349 | 7.833 | 9.073 | 6.749 | 6.949 |
| B | 8.555 | 8.980 | 10.066 | 9.276 | 18.970 | 8.098 | 10.555 |
| C | 173.48 | 19.911 | 43.376 | 22.29 | 39.914 | −17.453 | −18.408 |
| D | 17.04 | 19.280 | 28.979 | 20.89 | 34.31 | 20.592 | 22.063 |
| E | 5.688 | 5.978 | 6.645 | 6.16 | 7.361 | 5.365 | 5.562 |
| F | 9.229 | 9.769 | 11.188 | 10.144 | 12.975 | 8.940 | 9.433 |
| G | 10.182 | 11.668 | 15.23 | 12.50 | 23.56 | 11.743 | 14.042 |
| H | 7.469 | 8.12 | 9.93 | 8.58 | 12.44 | 7.783 | 8.476 |

However, in the dynamic regime, nanocluster **G** stands out as the most efficient across both frequencies, particularly at $\omega = 0.04282$ a.u., where it achieves the highest values of $\gamma(-\omega; \omega, 0, 0) = 12.50 \times 10^4$ a.u. and $\gamma(-2\omega; \omega, \omega, 0) = 23.56 \times 10^4$ a.u. These values indicate nanocluster **G**'s superior ability to mediate dynamic NLO processes. On the other hand, nanocluster **C**, despite its exceptional static performance, exhibits a significant drop in the dynamic second hyperpolarizability, with $\gamma(-\omega; \omega, 0, 0) = 19.911 \times 10^4$ a.u. and $\gamma(-2\omega; \omega, \omega, 0) = 39.914 \times 10^4$ a.u. at $\omega = 0.04282$ a.u., trailing behind clusters like **G** and **B**. Nanoclusters **E** and **A** showed the smallest dc-Kerr effect at $\omega = 0.034$ a.u. as well as at $\omega = 0.04282$ a.u., respectively. These results suggest that the third-order NLO response can be effectively enhanced by increasing the frequency of the incident light.

The degenerate four-wave mixing (DFWM) coefficients, $\gamma^{\text{DFWM}}$ ($\gamma(-\omega; \omega, -\omega, \omega)$), were calculated using the static, DC-Kerr, and ESHG second hyperpolarizability coefficients, and the results are presented in Fig. 16. The data reveal distinct NLO responses among the nanoclusters, with most exhibiting positive DFWM values, indicative of self-focusing behavior, except for nanocluster **C**, which displays significant negative values

$(-21.08 \times 10^4$ and $-22.23 \times 10^4$ a.u.), corresponding to strong self-defocusing effects.[90] The positive DFWM values of nanoclusters **D** and **G** are the largest, reaching $26.65 \times 10^4$ a.u. and $16.96 \times 10^4$ a.u. at $\omega = 0.042$ a.u., respectively, highlighting their potential for NLO applications such as optical switching and signal amplification. Nanoclusters **A**, **E**, **F**, and **H** show moderate positive values, while **B** exhibits an intermediate enhancement with increasing frequency. The DFWM values generally increase at higher frequencies, indicating frequency-dependent enhancement of the NLO response, except for nanocluster **C**, where negative values become slightly more pronounced, reinforcing its self-defocusing nature. The results underscore the variability in nonlinear optical behavior across the nanoclusters, with nanoclusters **D** and **G** being strong candidates for dynamic applications, while cluster **C** offers potential for niche uses requiring beam shaping or dispersion control.

The DFWM values and the quadratic nonlinear refractive index ($n_2$) of the nanoclusters exhibit the same trend (Table 14). At both frequencies, the largest $n_2$ values are observed for nanocluster **D** ($20.592 \times 10^{-18}$ cm$^2$ W$^{-1}$ and $22.063 \times 10^{-18}$ cm$^2$ W$^{-1}$) followed by **G** ($11.743 \times 10^{-18}$ and $14.042 \times 10^{-18}$ cm$^2$ W$^{-1}$). For nanoclusters **A**, **E**, and **F**, the $n_2$ values at $\omega = 0.034$ a.u. are $6.749 \times 10^{-18}$, $5.365 \times 10^{-18}$ and $8.940 \times 10^{-18}$ cm$^2$ W$^{-1}$, respectively. These values show a slight increase at the higher frequency ($\omega = 0.04282$ a.u.), demonstrating frequency dependence. Notably, the negative $n_2$ values for nanocluster **C** at both frequencies suggest a dominant one-photon resonance effect, possibly overshadowing two-photon resonance contributions, distinguishing it from the other clusters.[91,92]

### Influence of the solvent environment on the NLO responses of nanocluster A

To assess the influence of solvent environments on the NLO responses of nanocluster **A**, we computed its static polarizability, polarizability anisotropy, as well as its first and second hyperpolarizabilities in different solvents (water, benzene, and methanol) at the M06-2X/6-31+G(d)/SDD/CPCM level of theory. The corresponding results are summarized in Table 15.

The computed results reveal that the static polarizability ($\alpha$) of nanocluster **A** undergoes a significant enhancement upon solvation. The $\alpha$ value increases from 379 a.u. in the gas phase
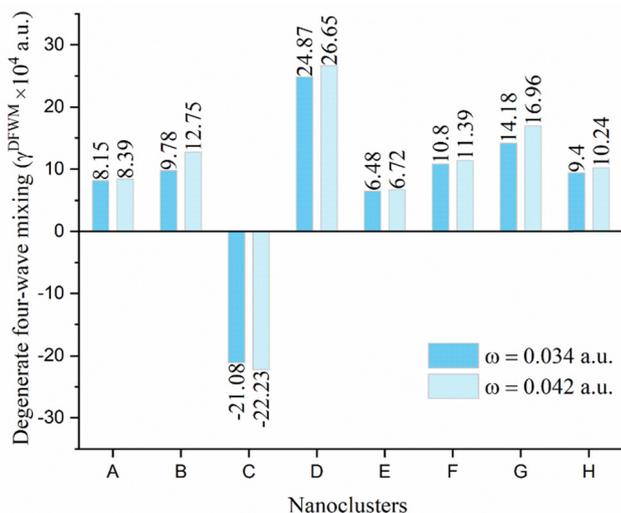


**Fig. 16** Variation in degenerate four-wave mixing coefficients for nanoclusters **A** to **H**.

**Table 15** Polarizability ($\alpha$), polarizability anisotropy ($\Delta\alpha$), and first and second hyperpolarizabilities ($\beta_{tot}^0$, $\beta_{HRS}^0$ and $\gamma(0; 0, 0, 0)$) calculated in the static regime in different solvents of nanocluster A ($\varepsilon$ dielectric constant)

| | Water ($\varepsilon = 78.355$) | Methanol ($\varepsilon = 32.613$) | Benzene ($\varepsilon = 2.270$) |
|---|---|---|---|
| $\alpha\,(0,0)$ | 807 | 802 | 605 |
| $\Delta\alpha\,(0,0)$ | 109 | 99 | 53 |
| $\beta_{tot}^0\,(0;0,0)$ | 6857 | 6221 | 2130 |
| $\beta_{HRS}^0\,(0;0,0)$ | 3609 | 3676 | 939 |
| $\gamma(0; 0, 0, 0)$ | $2.678 \times 10^6$ | $1.183 \times 10^6$ | $1.408 \times 10^6$ |

to 807 a.u. in water and 802 a.u. in methanol, reflecting the pronounced effect of polar solvents in promoting electronic delocalization and polarizability. On the other hand, the value obtained in benzene (605 a.u.) shows a moderate increase, which is consistent with the comparatively lower dielectric constant of this apolar solvent. The polarizability anisotropy ($\Delta\alpha$) exhibits a trend analogous to that of the static polarizability, with the maximum value observed in water (109 a.u.), indicative of pronounced directional electronic response in a highly polar medium. A significantly lower $\Delta\alpha$ value is obtained in benzene (53 a.u.), consistent with its reduced polarity and limited capacity to induce anisotropic polarization.

The first-order hyperpolarizability of compound **A** is significantly enhanced in solvent environments compared to the gas phase. In water, $\beta_{tot}$ increases from 203 a.u. to 6857 a.u., representing an enhancement by a factor of 34. Similarly, methanol enhances the first hyperpolarizability by approximately 31 times, while benzene results in an increase of about 10 times relative to the gas-phase value. This trend clearly demonstrates the impact of solvent polarity, with polar solvents exhibiting a greater ability to enhance second-order NLO responses compared to apolar media. Furthermore, the hyper-Rayleigh scattering hyperpolarizability ($\beta_{HRS}^0$) exhibits a comparable trend, increasing by approximately 17 times in polar solvents and 4 times in the apolar solvent (benzene), relative to its gas-phase value.

Regarding the second hyperpolarizability, the value of $\gamma(0; 0, 0, 0)$ in water is approximately 36 times higher than that in the gas phase, while in methanol and benzene, it is enhanced by factors of 16 and 19, respectively. These results clearly demonstrate the significant influence of solvation on the NLO behavior of the nanocluster **A**. We can conclude that solvent polarity plays a critical role in amplifying both second- and third-order NLO responses of nanocluster **A**. In a future study, we will investigate the effect of polar and nonpolar solvent environments on nanoclusters **B** to **H**.

## Conclusions

This paper presents a systematic DFT, TD-DFT, SOS, QTAIM and EDA-NOCV study on two series of hydride nanoclusters, $[Cu_3L_3(H)_i(BH_4)_j]^+$ and $[Cu_3L_2(H)_i(BH_4)_j]^+$ where $i = 0$ to 2 and $j = 0$ and 1. Quantum chemical calculations indicate that the presence of $BH_4$ and hydride fragments enhances the stability of $[Cu_3L_3(H)(BH_4)]^+$ ($\eta = 7.074$ eV), whereas $[Cu_3L_2(H)(BH_4)]^+$

exhibits lower stability ($\eta = 4.189$ eV). EDA-NOCV analysis reveals a significant covalent contribution to the bonding interaction between the copper centre and the ligand fragments. TD-DFT calculations confirm the near-infrared (NIR) transparency of these nanoclusters, with **A**, **B**, **E**, and **H** demonstrating exceptional optical transparency across both NIR and visible regions. Furthermore, introducing a single hydride unit significantly enhances second-order NLO responses compared to two hydride units or a hydride and $BH_4$. This is a result of modifications in the electronic topology and variations in kinetic and potential energy densities at BCP and RCP points. Notably, nanocluster **H** exhibits the highest first hyperpolarizability, attributed to greater kinetic energy within Cu–H bonds compared to **F**. Overall, SOS analysis reveals a direct correlation between dipole moment variations in crucial excited states and first hyperpolarizability. Frequency-dependent calculations at laser wavelengths of 1340 and 1064 nm indicate that the first hyperpolarizability in the dynamic regime is significantly larger than that in the static regime, and the electro-optical Pockels effect is more pronounced at shorter incident wavelengths. Additionally, nanocluster **D** exhibits the highest second-order hyperpolarizability ($173.48 \times 10^4$ a.u.), while **E** shows the lowest ($5.688 \times 10^4$ a.u.). The DFWM values suggest that nanoclusters **D** and **G** are strong candidates for dynamic applications. Copper hydride nanoclusters demonstrate broad applicability across various fields. This study unveils their potential as efficient second- and third-order nonlinear optical materials.

## Author contributions

Conceptualization and methodology: A. A., A. M., D. H. and H. C. Investigation: R. K. B., A. A., D. H., and A. M. Writing – original draft preparation: D. H. and H. C.; writing – review & editing: A. A., A. M., C. M., D. H. and H. C. Data curation: R. K. B., D. H. and A. A. All authors have read and agreed to the published version of the manuscript.

## Data availability

The data supporting this article have been included as part of the ESI.†

## Conflicts of interest

There are no conflicts to declare.

## Acknowledgements

# References

1 P. A. Franken, A. E. Hill, C. W. Peters and G. Weinreich, Generation of Optical Harmonics, *Phys. Rev. Lett.*, 1961, **7**, 118–120, DOI: **10.1103/PhysRevLett.7.118**.

2 G. Yu, X. Huang, S. Li and W. Chen, Theoretical Insights and Design of Intriguing Nonlinear Optical Species Involving the Excess Electron, *Int. J. Quantum Chem.*, 2015, **115**, 671–679, DOI: **10.1002/qua.24878**.

3 C. Andraud, F. Cyril, B. Olivier, H. Chermette and P. L. Baldeck, Excitonically Coupled Oligomers and Dendrimers for Two-Photon Absorption, *Adv. Polym. Sci.*, 2008, **214**, 149–203, DOI: **10.1007/12_2008_158**.

4 A. V. Kachynski, A. Pliss, A. N. Kuzmin, T. Y. Ohulchanskyy, A. Baev, J. Qu and P. N. Prasad, Photodynamic Therapy by in Situ Nonlinear Photon Conversion, *Nat. Photonics*, 2014, **8**, 455–461, DOI: **10.1038/nphoton.2014.90**.

5 V. Parodi, E. Jacchetti, R. Osellame, G. Cerullo, D. Polli and M. T. Raimondi, Nonlinear Optical Microscopy: From Fundamentals to Applications in Live Bioimaging, *Front. Bioeng. Biotechnol.*, 2020, **8**, 1–18, DOI: **10.3389/fbioe.2020.585363**.

6 G. Deka, C. K. Sun, K. Fujita and S. W. Chu, Nonlinear Plasmonic Imaging Techniques and Their Biological Applications, *Nanophotonics*, 2017, **6**, 31–49, DOI: **10.1515/nanoph-2015-0149**.

7 J. Roslund, R. M. De Araújo, S. Jiang, C. Fabre and N. Treps, Wavelength-Multiplexed Quantum Networks with Ultrafast Frequency Combs, *Nat. Photonics*, 2014, **8**, 109–112, DOI: **10.1038/nphoton.2013.340**.

8 J. Zyss and I. Ledoux, Nonlinear Optics in Multipolar Media: Theory and Experiments, *Chem. Rev.*, 1994, **94**(1), 77–105, DOI: **10.1021/cr00025a003**.

9 D. M. Burland, R. D. Miller and C. A. Walsh, Second-Order Nonlinearity in Poled-Polymer Systems, *Chem. Rev.*, 1994, **94**(1), 31–75, DOI: **10.1021/cr00025a002**.

10 T. Verbiest, S. Houbrechts, M. Kauranen, K. Clays and A. Persoons, Second-Order Nonlinear Optical Materials: Recent Advances in Chromophore Design, *J. Mater. Chem.*, 1997, **7**(11), 2175–2189, DOI: **10.1039/a703434b**.

11 S. Di Bella, Second-Order Nonlinear Optical Properties of Transition Metal Complexes, *Chem. Soc. Rev.*, 2001, **30**(6), 355–366, DOI: **10.1039/b100820j**.

12 S. R. Marder, Organic Nonlinear Optical Materials: Where We Have Been and Where We Are Going, *Chem. Commun.*, 2006, (No. 2), 131–134, DOI: **10.1039/b512646k**.

13 M. Zaidi, D. Hannachi and H. Chermette, Correlation between Second Ionization Potential and Nonlinear Optical Properties of Bivalent Transition-Metal Complexes: A Quantum Chemical Study, *Inorg. Chem.*, 2021, **60**, 6616–6632.

14 F. Chérioux, H. Maillotte, P. Audebert and J. Zyss, Synthesis and Characterisation of an Octupolar Polymer and New Molecular Octupoles with Off-Resonant Third Order Optical Nonlinearities, *Chem. Commun.*, 1999, (No. 20), 2083–2084, DOI: **10.1039/a905899k**.

15 M. Fontani, A. Colombo, C. Dragonetti, S. Righetto, D. Roberto and D. Marinotto, Cyclometalated Ir(III) Complexes with Curcuminoid Ligands as Active Second-Order Nlo Chromophores and Building Blocks for Shg Polymeric Films, *Inorganics*, 2020, **8**(36), 1–12, DOI: **10.3390/INORGANICS8050036**.

16 S. J. Wang, Y. F. Wang and C. Cai, Multidecker Sandwich Cluster $V_n Ben_{n+1}$ ($n$ = 1, 2, 3, 4) as a Polarizable Bridge for Designing 1D Second-Order NLO Chromophore: Metal-$\pi$ Sandwich Multilayer Structure as a Particular Charge-Transfer Axis for Constructing Multidimensional NLO Molecules, *J. Phys. Chem. C*, 2015, **119**, 16256–16262, DOI: **10.1021/acs.jpcc.5b04656**.

17 S. J. Wang, Y. F. Wang and C. Cai, Multidecker Sandwich Complexes $V_n Ben_{n+1}$ ($n$ = 1, 2, 3) as Stronger Electron Donor Relative to Ferrocene for Designing High-Performance Organometallic Second-Order Nlo Chromophores: Evident Layer Effect on the First Hyperpolarizability and Two-Dimensional N, *J. Phys. Chem. C*, 2015, **119**, 5589–5595, DOI: **10.1021/jp5123272**.

18 M. Zaidi, D. Hannachi, N. Chaouia and H. Chermette, Understanding the Second and Third Order Nonlinear Optical Responses of $M@b_{66/64}Al_{12}N_{12}$: A Comprehensive DFT and TD-DFT Study, *New J. Chem.*, 2024, **48**, 11812–11828, DOI: **10.1039/d4nj01849d**.

19 C. Y. Liu, S. F. Yuan, S. Wang, Z. J. Guan, D. E. Jiang and Q. M. Wang, Structural Transformation and Catalytic Hydrogenation Activity of Amidinate-Protected Copper Hydride Clusters, *Nat. Commun.*, 2022, **13**, 1–8, DOI: **10.1038/s41467-022-29819-y**.

20 A. Wurtz, Sur l'hydrure de Cuivre, *C. R. Hebd. Seances Acad. Sci., Ser. D*, 1844, **18**, 702–704.

21 B. H. Lee, C. C. Wu, X. Fang, C. W. Liu and J. L. Zhu, [Cu8(M8-H){S2P (OEt)2}6](PF6): A Novel Catalytic Hydride-Centered Copper Cluster for Azide-Alkyne Cycloaddtion, *Catal. Lett.*, 2013, **143**, 572–577, DOI: **10.1007/s10562-013-0993-7**.

22 E. C. A. Hydroamination, S. Zhu and S. L. Buchwald, Enantioselective CuH-Catalyzed Anti-Markovnikov Hydroamination of 1,1-Disubstituted Alkenes, *J. Am. Chem. Soc.*, 2014, **136**, 15913–15916.

23 S. Zhu, N. Niljianskul and S. L. Buchwald, A Direct Approach to Amines with Remote Stereocentres by Enantioselective CuH-Catalysed Reductive Relay Hydroamination, *Nat. Chem.*, 2016, **8**, 144–150, DOI: **10.1038/nchem.2418**.

24 M. R. Uehling, A. M. Suess and G. Lalic, Copper-Catalyzed Hydroalkylation of Terminal Alkynes, *J. Am. Chem. Soc.*, 2015, **137**, 1424–1427, DOI: **10.1021/ja5124368**.

25 D. Noh, H. Chea, J. Ju and J. Yun, Highly Regio- and Enantioselective Copper-Catalyzed Hydroboration of Styrenes, *Angew. Chem., Int. Ed.*, 2009, **48**, 6062–6064, DOI: **10.1002/anie.200902015**.

26 R. Shintani and K. Nozaki, Copper-Catalyzed Hydroboration of Carbon Dioxide, *Organometallics*, 2013, **32**, 2459–2462, DOI: **10.1021/om400175h**.

27 J.-H. Liao, R. S. Dhayal, X. Wang, S. Kahlal, J.-Y. Saillard and C. W. Liu, Neutron Diffraction Studies of a Four-Coordinated Hydride in Near Square-Planar Geometry, *Inorg. Chem.*, 2014, **53**, 11140–11145.

28  K. Motokura, D. Kashiwame, N. Takahashi, A. Miyaji and T. Baba, Highly Active and Selective Catalysis of Copper Diphosphine Complexes for the Transformation of Carbon Dioxide into Silyl Formate, *Chem. – Eur. J.*, 2013, **19**, 10030–10037, DOI: **10.1002/chem.201300935**.

29  P. Liao, C. Fang, A. J. Edwards, S. Kahlal, J.-Y. Saillard and C. W. Liu, Hydrido Copper Clusters Supported by Dithio-carbamates: Oxidative Hydride Removal and Neutron Diffraction Analysis of $[Cu_7(H)\{S_2C(Aza-15-Crown-5)\}_6]$, *Inorg. Chem.*, 2012, **7**, 6577–6591.

30  K. Nakamae, B. Kure, T. Nakajima, Y. Ura and T. Tanase, Facile Insertion of Carbon Dioxide into $Cu_2(\mu$-H) Dinuclear Units Supported by Tetraphosphine Ligands, *Chem. – Asian J.*, 2014, **9**, 3106–3110, DOI: **10.1002/asia.201402900**.

31  C. Sun, N. Mammen, S. Kaappa, P. Yuan, G. Deng, C. Zhao, J. Yan, S. Malola, K. Honkala, H. Häkkinen, B. K. Teo and N. Zheng, Atomically Precise, Thiolated Copper-Hydride Nanoclusters as Single-Site Hydrogenation Catalysts for Ketones in Mild Conditions, *ACS Nano*, 2019, **13**, 5975–5986, DOI: **10.1021/acsnano.9b02052**.

32  H. Shen, L. Wang, O. López-Estrada, C. Hu, Q. Wu, D. Cao, S. Malola, B. K. Teo, H. Häkkinen and N. Zheng, Copper-Hydride Nanoclusters with Enhanced Stability by N-Heterocyclic Carbenes, *Nano Res.*, 2021, **14**, 3303–3308, DOI: **10.1007/s12274-021-3389-9**.

33  X. Zheng, Y. Liu, W. Ma, Y. Su and Y. Wang, The Structure-Activity Relationship of Copper Hydride Nanoclusters in Hydrogenation and Reduction Reactions, *Nanoscale Adv.*, 2024, **6**(5), 1374–1379, DOI: **10.1039/d3na01145c**.

34  J. Li, J. M. White, R. J. Mulder, G. E. Reid, P. S. Donnelly and R. A. J. O'Hair, Synthesis, Structural Characterization, and Gas-Phase Unimolecular Reactivity of Bis(Diphenylphos-phino)Amino Copper Hydride Nanoclusters $[Cu_3(X)(\mu_3$-H)-$((PPh_2)_2NH)_3](BF_4)$, Where X = M2-Cl and M3-BH4, *Inorg. Chem.*, 2016, **55**, 9858–9868, DOI: **10.1021/acs.inorgchem.6b01696**.

35  Y. Zhao and D. G. Truhlar, The M06 Suite of Density Functionals for Main Group Thermochemistry, Thermochemical Kinetics, Noncovalent Interactions, Excited States, and Transition Elements: Two New Functionals and Systematic Testing of Four M06-Class Functionals and 12 Other Function, *Theor. Chem. Acc.*, 2008, **120**, 215–241, DOI: **10.1007/s00214-007-0310-x**.

36  A. M. Arif, A. Yousaf, H. L. Xu and Z. M. Su, *N*-(*O*-Methoxy-phenyl)Aza-15-Crown-5-Ether Derivatives: Highly Efficient and Wide Range Nonlinear Optical Response Based Cation Recognition, *J. Mol. Liq.*, 2020, **301**, 22–24, DOI: **10.1016/j.molliq.2020.112492**.

37  A. Sajjad, S. Sarfaraz, A. Ahsan, I. Bayach, M. H. S. A. Hamid, N. S. Sheikh and K. Ayub, Theoretical Study of Dodeca-fluorophenylene-Based Superalkalides with Significantly High NLO Response, *ACS Omega*, 2023, **8**, 45589–45598, DOI: **10.1021/acsomega.3c05791**.

38  A. Shokuhi Rad and K. Ayub, Substitutional Doping of Zirconium-, Molybdenum-, Ruthenium-, and Palladium: An Effective Method to Improve Nonlinear Optical and

Electronic Property of C20 Fullerene, *Comput. Theor. Chem.*, 2017, **1121**, 68–75, DOI: **10.1016/j.comptc.2017.10.015**.

39  B. Zhang, J. Wen, Y. Zhang, Y. Xiong, X. Huang, J. Hou, X. Wang, J. Guan and Q. Zhi, Design a Novel Type of Excess Electron Compounds with Large Nonlinear Optical Responses Using Group 12 Elements (Zn, Cd and Hg), *J. Mol. Graphics Modell.*, 2021, **109**, 108003, DOI: **10.1016/j.jmgm.2021.108003**.

40  A. Ahsin, A. Ali and K. Ayub, Alkaline Earth Metals Serving as Source of Excess Electron for Alkaline Earth Metals to Impart Large Second and Third Order Nonlinear Optical Response; a DFT Study, *J. Mol. Graphics Modell.*, 2020, **101**, 107759, DOI: **10.1016/j.jmgm.2020.107759**.

41  G. A. Petersson and A. A.-L. Mohammad, A Complete Basis Set Model Chemistry. II. The Total Energies of Open-Shell Atoms and Hydrides of the First-Row Atoms, *J. Chem. Phys.*, 1991, **9**, 6081–6090, DOI: **10.1063/1.460447**.

42  G. A. Petersson, A. Bennett, T. G. Tensfeldt, M. A. Al-Laham, W. A. Shirley and J. Mantzaris, A Complete Basis Set Model Chemistry. I. The Total Energies of Closed-Shell Atoms and Hydrides of the First-Row Elements, *J. Chem. Phys.*, 1988, **89**, 2193–2218, DOI: **10.1063/1.455064**.

43  M. J. Frisch, G. W. Trucks, H. B. Schlegel, G. E. Scuseria, M. A. Robb, J. R. Cheeseman, G. Scalmani, V. Barone, G. A. Petersson, H. Nakatsuji, X. Li, M. Caricato, A. V. Marenich, J. Bloino, B. G. Janesko, R. Gomperts and B. Mennucci, *et al.*, *Gaussian 16, Revis. A.03*, Gaussian, Inc., Wallingford.

44  G. Te Velde, F. M. Bickelhaupt, E. J. Baerends, C. Fonseca Guerra, S. J. A. Van Gisbergen, J. G. Snijders and T. Ziegler, Chemistry with ADF, *J. Comput. Chem.*, 2001, **22**, 931–967.

45  R. F. W. Bader, T. T. Nguyendang and Y. Tal, Quantum Topology of Molecular Charge Distributions. II. Molecular Structure and Its Change Quantum Topology of Molecular Charge Distributions. II. Molecular Structure and Its Change, *J. Chem. Phys.*, 1979, **4316**, 4316, DOI: **10.1063/1.438006**.

46  R. F. W. Bader, T. T. Nguyen-Dang and Y. Tal, Quantum Topology of Molecular Charge Distributions. II. Molecular Structure and Its Change, *J. Chem. Phys.*, 1979, **70**(9), 4316–4329, DOI: **10.1063/1.438006**.

47  R. F. W. Bader, A Quantum Theory of Molecular Structure and Its Applications, *Chem. Rev.*, 1991, **91**(5), 893–928, DOI: **10.1021/cr00005a013**.

48  P. S. V. Kumar, V. Raghavendra and V. Subramanian, Bader's Theory of Atoms in Molecules (AIM) and Its Applications, *J. Chem. Sci.*, 2016, **128**, 1527–1536, DOI: **10.1007/s12039-016-1172-3**.

49  P. Jerabek, P. Schwerdtfeger and G. Frenking, Dative and Electron-Sharing Bonding in Transition Metal Compounds, *J. Comput. Chem.*, 2019, **40**, 247–264, DOI: **10.1002/jcc.25584**.

50  M. P. Mitoraj, M. G. Babashkina, K. Robeyns, F. Sagan, D. W. Szczepanik, Y. V. Seredina, Y. Garcia and D. A. Safin, Chameleon-like Nature of Anagostic Interactions and Its Impact on Metalloaromaticity in Square-Planar Nickel Complexes, *Organometallics*, 2019, **38**, 1973–1981, DOI: **10.1021/acs.organomet.9b00062**.

51 P. P. John and M. E. Kieron Burke, Generalized Gradient Approximation Made Simple John, *Phys. Rev. Lett.*, 1996, **77**, 3865–3868, DOI: **10.1103/PhysRevLett.77.3865**.

52 A. D. Becke, A Multicenter Numerical Integration Scheme for Polyatomic Molecules, *J. Chem. Phys.*, 1988, **88**(4), 2547–2553, DOI: **10.1063/1.454033**.

53 D. Hannachi, M. F. Haroun, A. Khireddine and H. Chermette, Optical and Nonlinear Optical Properties of Ln(Tp)₂, Where Ln = La,...,Lu and Tp = Tris(Pyrazolyl)-Borate: A DFT+TD-DFT Study, *New J. Chem.*, 2019, **43**, 14377–14389, DOI: **10.1039/c9nj03232k**.

54 E. Van Lenthe, Geometry Optimizations in the Zero Order Regular Approximation for Relativistic Effects, *J. Chem. Phys.*, 1999, **110**, 8943–8953, DOI: **10.1063/1.478813**.

55 J. E. Rice, R. D. Amos, S. M. Colwell, N. C. Handy and J. Sanz, Frequency Dependent Hyperpolarizabilities with Application to Formaldehyde and Methyl Fluoride, *J. Chem. Phys.*, 1990, **93**(12), 8828–8839, DOI: **10.1063/1.459221**.

56 H. Li, H. Xu, X. Shen, K. Han, Z. Bi and R. Xu, Size-, Electric-Field-, and Frequency-Dependent Third-Order Nonlinear Optical Properties of Hydrogenated Silicon Nanoclusters, *Sci. Rep.*, 2016, **6**, 28067, DOI: **10.1038/srep28067**.

57 H. A. Kurtz, J. J. P. Stewart and K. M. Dieter, Calculation of the Nonlinear Optical Properties of Molecules, *J. Comput. Chem.*, 1990, **11**(1), 82–87, DOI: **10.1002/jcc.540110110**.

58 D. P. Shelton and J. E. Rice, Measurements and Calculations of the Hyperpolarizabilities of Atoms and Small Molecules in the Gas Phase, *Chem. Rev.*, 1994, **94**(1), 3–29, DOI: **10.1021/cr00025a001**.

59 C. Brée, A. Demircan and G. Steinmeyer, Method for Computing the Nonlinear Refractive Index via Keldysh Theory, *IEEE J. Quantum Electron.*, 2010, **46**(4), 433–437, DOI: **10.1109/JQE.2009.2031599**.

60 M. Tarazkar, D. A. Romanov and R. J. Levis, Higher-Order Nonlinearity of Refractive Index: The Case of Argon, *J. Chem. Phys.*, 2014, **140**, 214316, DOI: **10.1063/1.4880716**.

61 A. Plaquet, M. Guillaume, B. Champagne, F. Castet, L. Ducasse, J. L. Pozzo and V. Rodriguez, In Silico Optimization of Merocyanine-Spiropyran Compounds as Second-Order Nonlinear Optical Molecular Switches, *Phys. Chem. Chem. Phys.*, 2008, **10**(41), 6223–6232, DOI: **10.1039/b806561f**.

62 N. Hou, R. Feng and X. H. Fang, A Theoretical Comparison of the Electrical and Nonlinear Optical Properties of GDY–π–TPA: The Important Role of π-Conjugated Bridge, *Int. J. Quantum Chem.*, 2022, **122**(19), 1–14, DOI: **10.1002/qua.26965**.

63 D. Kamli, D. Hannachi, D. Samsar and H. Chermette, Bis-TTF-Ge Derivatives: Promising Linear and Nonlinear Optical Properties, a Theoretical Investigation, *New J. Chem.*, 2023, **47**, 1234–1246, DOI: **10.1039/d2nj03671a**.

64 T. Lu and F. Chen, Multiwfn: A Multifunctional Wavefunction Analyzer, *J. Comput. Chem.*, 2012, **33**, 580–592, DOI: **10.1002/jcc.22885**.

65 M. Cossi, N. Rega, G. Scalmani and V. Barone, Energies, Structures, and Electronic Properties of Molecules in Solution with the C-PCM Solvation Model, *J. Comput. Chem.*, 2003, **24**, 669–681, DOI: **10.1002/jcc.10189**.

66 V. Barone and M. Cossi, Conductor Solvent Model, *J. Phys. Chem. A*, 1998, **102**(97), 1995–2001.

67 L. M. G. Abegaõ, R. D. Fonseca, F. A. Santos, J. J. Rodrigues, K. Kamada, C. R. Mendonca, S. Piguel and L. De Boni, First Molecular Electronic Hyperpolarizability of Series of π-Conjugated Oxazole Dyes in Solution: An Experimental and Theoretical Study, *RSC Adv.*, 2019, **9**(45), 26476–26482, DOI: **10.1039/c9ra05246a**.

68 A. M. Elhorri and M. Zouaoui-Rabah, NLO Response of Derivatives of Benzene, Stilbene and Diphenylacetylene: MP2 and DFT Calculations, *Chin. J. Chem. Eng.*, 2017, **25**, 800–808, DOI: **10.1016/j.cjche.2016.09.001**.

69 A. S. Tiwary, K. Datta and A. K. Mukherjee, Performance of the M06 Family of Functionals in Predicting the Charge Transfer Transition Energies of Molecular Complexes of TCNE with a Series of Methylated Indoles, *Comput. Theor. Chem.*, 2015, **1068**, 123–127, DOI: **10.1016/j.comptc.2015.06.033**.

70 P. K. Chattaraj and R. G. Parr, Density Functional Theory of Chemical Reactivity, *Struct. Bonding*, 1993, **80**, 151–174, DOI: **10.1039/9781782620112-00151**.

71 P. Mondal, K. K. Hazarika and R. C. Deka, Reactivity of α,β-Unsaturated Carbonyl Compounds towards Nucleophilic Addition Reaction: A Local Hard-Soft Acid-Base Approach, *PhysChemComm*, 2003, **6**(6), 24–27, DOI: **10.1039/b301675g**.

72 P. Geerlings, F. De Proft and W. Langenaeker, Conceptual Density Functional Theory, *Chem. Rev.*, 2003, **103**(5), 1793–1873, DOI: **10.1021/cr990029p**.

73 H. Chermette, Chemical Reactivity Indexes in Density Functional Theory, *J. Comput. Chem.*, 1999, **20**, 129–154, DOI: **10.1002/(SICI)1096-987X(19990115)20:1<129::AID-JCC13>3.0.CO;2-A**.

74 R. F. W. Bader, Atoms-in-Molecules, *Acc. Chem.*, 1985, **18**(1), 9–15, DOI: **10.1021/ar00109a003**.

75 P. S. V. Kumar, V. Raghavendra and V. Subramanian, Bader's Theory of Atoms in Molecules (AIM) and Its Applications to Chemical Bonding, *J. Chem. Sci.*, 2016, **128**(10), 1527–1536, DOI: **10.1007/s12039-016-1172-3**.

76 D. Hannachi, N. Ouddai, M. Arotçaréna and H. Chermette, Addition-Fragmentation Reaction of Thionoesters Compounds in Free-Radical Polymerisation (Methyl, Cyanomethyl and Styryl): A Theoretical Interpretation, *Mol. Phys.*, 2015, **113**(13–14), 1541–1550, DOI: **10.1080/00268976.2014.985275**.

77 E. J. Baerends, T. Ziegler, A. J. Atkins, J. Autschbach, O. Baseggio, D. Bashford, A. Bérces, F. M. Bickelhaupt, C. Bo, P. M. Boerrigter, C. Cappelli, L. Cavallo, C. Daul, D. P. Chong, D. V. Chulhai, L. Deng, R. M. Dickson, J. M. Dieterich, F. Egidi, D. E. Ellis, M. van Faassen, L. Fan, T. H. Fischer, A. Förster, C. Fonseca Guerra, M. Franchini, A. Ghysels, A. Giammona, S. J. A. van Gisbergen, A. Goez, A. W. Götz, J. A. Groeneveld, O. V. Gritsenko, M. Grüning, S. Gusarov, F. E. Harris, P. van den Hoek, Z. Hu, C. R. Jacob, H. Jacobsen, L. Jensen, L. Joubert, J. W. Kaminski, G. van

Kessel, C. König, F. Kootstra, A. Kovalenko, M. V. Krykunov, P. Lafiosca, E. van Lenthe, D. A. McCormack, M. Medves, A. Michalak, M. Mitoraj, S. M. Morton, J. Neugebauer, V. P. Nicu, L. Noodleman, V. P. Osinga, S. Patchkovskii, M. Pavanello, C. A. Peeples, P. H. T. Philipsen, D. Post, C. C. Pye, H. Ramanantoanina, P. Ramos, W. Ravenek, M. Reimann, J. I. Rodríguez, P. Ros, R. Rüger, P. R. T. Schipper, D. Schlüns, H. van Schoot, G. Schreckenbach, J. S. Seldenthuis, M. Seth, J. G. Snijders, M. Solà, M. Stener, M. Swart, D. Swerhone, V. Tognetti, G. te Velde, P. Vernooijs, L. Versluis, L. Visscher, O. Visser, F. Wang, T. A. Wesolowski, E. M. van Wezenbeek, G. Wiesenekker, S. K. Wolff, T. K. Woo and A. L. Yakovlev, *ADF, SCM*, Theoretical Chemistry, Vrije Universiteit, Amsterdam, The Netherlands, 2016, **https://www.scm.com**.

78  I. Rozas and I. Alkorta, Behavior of Ylides Containing N, O, and C Atoms as Hydrogen Bond Acceptors, *J. Am. Chem. Soc.*, 2000, **122**, 11154–11161.

79  S. Lakehal, A. Lakehal, M. Bouchagour and C. Morell, Combined QTAIM and ETS-NOCV Investigation of the Interactions in $Cl_nM[PhB(NtBu)_2]$ Complexes with M = Si & Ge ($n = 0$), As & Sb ($n = 1$), Te & Po ($n = 2$), *J. Mol. Model.*, 2018, **24**, 327, DOI: **10.1007/s00894-018-3852-z**.

80  L. Bondì, A. L. Garden, P. Jerabek, F. Totti and S. Brooker, Quantitative and Chemically Intuitive Evaluation of the Nature of M–L Bonds in Paramagnetic Compounds: Application of EDA-NOCV Theory to Spin Crossover Complexes, *Chem. – Eur. J.*, 2020, **26**, 13677–13685, DOI: **10.1002/chem.202002146**.

81  H. Abdoul-Carime, B. Farizon, M. Farizon, J. C. Mulatier, J. P. Dutasta and H. Chermette, Solution vs. Gas Phase Relative Stability of the Choline/Acetylcholine Cavitand Complexes, *Phys. Chem. Chem. Phys.*, 2015, **17**, 4448–4457, DOI: **10.1039/c4cp05354k**.

82  T. Ziegler and A. Rauk, Carbon Monoxide, Carbon Monosulfide, Molecular Nitrogen, Phosphorus Trifluoride, and Methyl Isocyanide as.Sigma. Donors and.Pi. Acceptors. A Theoretical Study by the Hartree-Fock-Slater Transition-State Method, *Inorg. Chem.*, 1979, **18**, 1755–1759, DOI: **10.1021/ic50197a006**.

83  T. Ziegler and A. Rauk, A Theoretical Study of the Ethylene-Metal Bond in Complexes between $Cu^+$, $Ag^+$, $Au^+$, $Pt^0$, or $Pt^{2+}$ and Ethylene, Based on the Hartree-Fock-Slater Transition-State Method, *Inorg. Chem.*, 1979, **18**, 1558–1565, DOI: **10.1021/ic50196a034**.

84  A. Michalak, M. Mitoraj and T. Ziegler, Bond Orbitals from Chemical Valence Theory, *J. Phys. Chem. A*, 2008, **112**, 1933–1939, DOI: **10.1021/jp075460u**.

85  M. Mitoraj and A. Michalak, Applications of Natural Orbitals for Chemical Valence in a Description of Bonding in Conjugated Molecules, *J. Mol. Model.*, 2008, **14**, 681–687, DOI: **10.1007/s00894-008-0276-1**.

86  C. Herliette, A. Alongamo and N. K. Nkungli, DFT-Based Study of the Impact of Transition Metal Coordination on the Charge Transport and Nonlinear Optical (NLO) Properties, *Mol. Phys.*, 2019, **117**(18), 2577–2592, DOI: **10.1080/00268976.2019.1576932**.

87  M. R. Maina, Y. Okamoto, K. Hamada, A. Okada, S. I. Nakashiba and N. Nishi, Effects of Superposition of 532 Nm and 1064 Nm Wavelengths in Copper Micro-Welding by Pulsed Nd:YAG Laser, *J. Mater. Process. Technol.*, 2022, **299**, DOI: **10.1016/j.jmatprotec.2021.117388**.

88  J. L. Oudar and D. S. Chemla, Hyperpolarizabilities of the Nitroanilines and Their Relations to the Excited State Dipole Moment, *J. Chem. Phys.*, 1976, **66**, 2664–2668, DOI: **10.1063/1.434213**.

89  J. L. Oudar, Optical Nonlinearities of Conjugated Molecules. Stilbene Derivatives and Highly Polar Aromatic Compounds, *J. Chem. Phys.*, 1977, **67**, 446–457, DOI: **10.1063/1.434888**.

90  C. E. Powell, M. G. Humphrey, M. P. Cifuentes, J. P. Morrall, M. Samoc and B. Luther-Davies, Organometallic Complexes for Nonlinear Optics. 33. Electrochemical Switching of the Third-Order Nonlinearity Observed by Simultaneous Femtosecond Degenerate Four-Wave Mixing and Pump–Probe Measurements, *J. Phys. Chem. A*, 2003, **107**, 11264–11266, DOI: **10.1021/jp0366217**.

91  M. Das Sumit Naskara, The Effect of Metal-to-Ligand Charge Transfer on Linear and Nonlinear Optical Properties of Hexaphyrin and Metallo-Hexaphyrins, *Mol. Phys.*, 2024, e2386385, DOI: **10.1080/00268976.2024.2386385**.

92  G. Stegeman, M. Kuzyk, D. G. Papazoglou and S. Tzortzakis, Off-Resonance and Non-Resonant Dispersion of Kerr Nonlinearity for Symmetric Molecules, *Opt. Express*, 2011, (No. 23), 22486, DOI: **10.1364/oe.19.022486**.